

Experimental realisation of the topological Haldane model

Gregor Jotzu, Michael Messer, Rémi Desbuquois, Martin Lebrat,
Thomas Uehlinger, Daniel Greif & Tilman Esslinger
Institute for Quantum Electronics, ETH Zurich, 8093 Zurich, Switzerland
(Dated: July 1, 2014)

PACS numbers: 03.75.Ss, 67.85.Lm, 03.65.Vf, 73.43.-f, 73.43.Nq, 71.10.Fd, 73.22.Pr

The Haldane model on the honeycomb lattice is a paradigmatic example of a Hamiltonian featuring topologically distinct phases of matter [1]. It describes a mechanism through which a quantum Hall effect can appear as an intrinsic property of a band-structure, rather than being caused by an external magnetic field [2]. Although an implementation in a material was considered unlikely, it has provided the conceptual basis for theoretical and experimental research exploring topological insulators and superconductors [2–6]. Here we report on the experimental realisation of the Haldane model and the characterisation of its topological band-structure, using ultracold fermionic atoms in a periodically modulated optical honeycomb lattice. The model is based on breaking time-reversal symmetry as well as inversion symmetry. The former is achieved through the introduction of complex next-nearest-neighbour tunnelling terms, which we induce through circular modulation of the lattice position [7]. For the latter, we create an energy offset between neighbouring sites [8]. Breaking either of these symmetries opens a gap in the band-structure, which is probed using momentum-resolved interband transitions. We explore the resulting Berry-curvatures of the lowest band by applying a constant force to the atoms and find orthogonal drifts analogous to a Hall current. The competition between both broken symmetries gives rise to a transition between topologically distinct regimes. By identifying the vanishing gap at a single Dirac point, we map out this transition line experimentally and compare it to calculations using Floquet theory without free parameters. We verify that our approach, which allows for dynamically tuning topological properties, is suitable even for interacting fermionic systems. Furthermore, we propose a direct extension to realise spin-dependent topological Hamiltonians.

In a honeycomb lattice symmetric under time-reversal and inversion, the two lowest bands are connected at two Dirac points. Each broken symmetry leads to a gapped energy-spectrum. F. D. M. Haldane realised that the resulting phases are topologically distinct: A broken inversion symmetry (IS), caused by an energy offset between

the two sublattices, leads to a trivial band-insulator at half-filling. Time-reversal symmetry (TRS) can be broken by complex next-nearest-neighbour tunnel couplings (Fig. 1a). The corresponding staggered magnetic fluxes

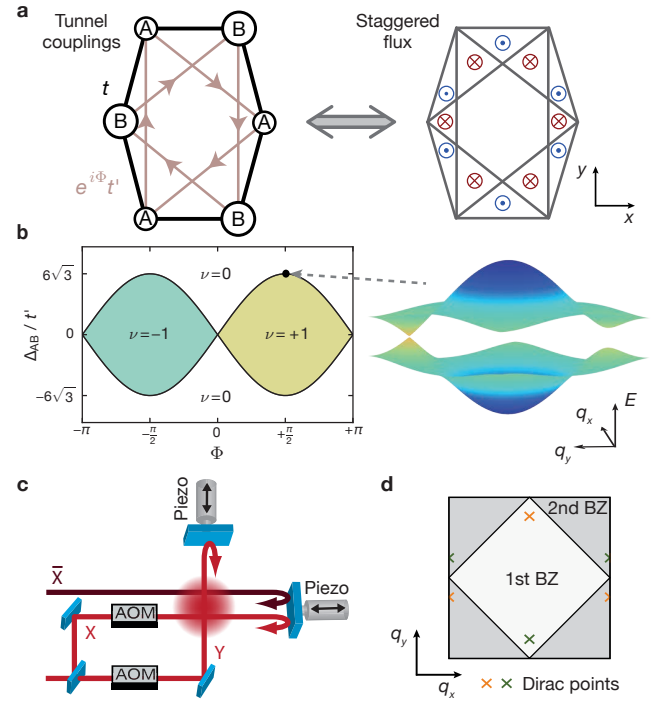


FIG. 1: **Experimental realisation of the Haldane model.** **a**, Tight-binding model of the honeycomb lattice realised in the experiment. An energy offset Δ_{AB} between sublattice A and B breaks inversion symmetry (IS). Nearest-neighbour tunnel couplings t are real-valued, whereas next-nearest-neighbour tunnelling $e^{i\Phi}t'$ carries tunable phases indicated by arrows. Corresponding staggered magnetic fluxes (sketched on the right) sum up to zero but break time-reversal symmetry (TRS). **b**, Topological regimes of the Haldane model, for isotropic t and t' . The trivial (Chern number $\nu = 0$) and Chern-insulating ($\nu = \pm 1$) regimes are connected by topological transitions (black lines), where the band-structure (shown on the right) becomes gapless at a single Dirac point. **c**, Laser beam set-up forming the optical lattice. \bar{X} is frequency-detuned from the other beams. Piezoelectric actuators sinusoidally modulate the retro-reflecting mirrors, with a controllable phase difference φ . Acousto-optic modulators (AOMs) ensure the stability of the lattice geometry (Methods). **d**, Resulting Brillouin-zones (BZs) featuring two Dirac-points.

sum up to zero in one unit-cell, thereby preserving the translation symmetry of the lattice. This gives rise to a topological Chern-insulator, where a non-zero Hall conductance appears despite the absence of a net magnetic field [1, 2]. When both symmetries are broken, a topological phase transition connects two regimes with a distinct topological invariant, the Chern number, which changes from 0 to ± 1 , see Fig. 1b. There, the gap closes at a single Dirac point. These transitions have attracted great interest, as they cannot be described by Landau's theory of phase transitions, owing to the absence of a changing local order parameter [6].

A crucial experimental challenge for the realisation of the Haldane model is the creation of complex next-nearest-neighbour tunnelling. Here we show that this becomes possible with ultracold atoms in optical lattices periodically modulated in time. So far, pioneering experiments with bosons showed a renormalization of existing tunnelling amplitudes in one dimension [9, 10], and were extended to control tunnelling phases [11, 12] and higher-order tunnelling [13]. In higher dimensions this allowed for studying phase transitions [14, 15], and topologically trivial staggered fluxes were realised [16, 17]. Furthermore, uniform flux configurations were observed using rotation and laser-assisted tunnelling [18, 19], although for the latter method, heating seemed to prevent the observation of a flux in some experiments [20]. In a honeycomb lattice, a rotating force can induce the required complex tunnelling, as recognised by T. Oka and H. Aoki [7]. Using photonic crystal fibres, a classical version of this proposal was used to study topologically protected edge modes in the inversion-symmetric regime [21]. We access the full parameter space of the Haldane model using a fermionic quantum gas, by extending the proposal to elliptical modulation of the lattice position and additionally breaking IS through a deformation of the lattice geometry.

The starting point of our experiment is a non-interacting, ultracold gas of 4×10^4 to 6×10^4 fermionic ^{40}K atoms prepared in the lowest band of a honeycomb optical lattice created by several laser beams at wavelength $\lambda = 1064\text{ nm}$, arranged in the $x - y$ plane as depicted in Fig. 1c and detailed in [8]. The two lowest bands have a total bandwidth of $\hbar \times 3.9(1)\text{ kHz}$, with a gap of $\hbar \times 5.4(2)\text{ kHz}$ to the next higher band, and contain two Dirac points at opposite quasi-momenta, see Fig. 1d. Here \hbar denotes Planck's constant. After loading the atoms into the honeycomb lattice, we ramp on a sinusoidal modulation of the lattice position along the x and y directions with amplitude $0.087(1)\lambda$, frequency 4.0 kHz and phase difference φ . This gives access to linear, circular and elliptical trajectories.

The effective Hamiltonian of our system in the phase-modulated honeycomb lattice is computed using analytical and numerical Floquet theory (See Methods and [Supplementary Material](#) for a detailed discussion). It is well

described by the Haldane model [1]

$$\hat{H} = \sum_{\langle ij \rangle} t_{ij} \hat{c}_i^\dagger \hat{c}_j + \sum_{\langle\langle ij \rangle\rangle} e^{i\Phi_{ij}} t'_{ij} \hat{c}_i^\dagger \hat{c}_j + \Delta_{AB} \sum_{i \in A} \hat{c}_i^\dagger \hat{c}_i, \quad (1)$$

where t_{ij} and t'_{ij} are real-valued nearest- and next-nearest-neighbour tunnelling amplitudes, and the latter contain additional complex phases Φ_{ij} defined along the arrows shown in Fig. 1a. The fermionic creation and annihilation operators are denoted by \hat{c}_i^\dagger and \hat{c}_i . The energy offset $\Delta_{AB} \geq 0$ between sites of the A and B sublattice breaks IS and opens a gap $|\Delta_{AB}|$ [8]. TRS can be broken by changing φ . This controls the imaginary part of the next-nearest-neighbour tunnelling, whereas its real part as well as t_{ij} and Δ_{AB} are mostly unaffected (Methods). Breaking only TRS opens an energy gap $|\Delta_T|$ at the Dirac points given by a sum of three tunnel couplings t'_l connecting the same sublattice

$$\Delta_T = \Delta_T^{\max} \sin(\varphi) = - \sum_l w_l t'_l \sin(\Phi_l), \quad (2)$$

with weights w_l depending on the lattice geometry. For our parameters circular modulation ($\varphi = \pm 90^\circ$) leads to a maximum gap of $\hbar \times 88^{+10}_{-34}\text{ Hz}$, whereas the gap vanishes for linear modulation ($\varphi = 0^\circ, \pm 180^\circ$), where TRS is preserved.

In order to probe the opening of gaps in the system, we drive Landau-Zener transitions through the Dirac points [8, 22]. Applying a constant force along the x -direction by means of a magnetic field gradient causes an energy offset $E/\hbar = 103.6(1)\text{ Hz}$ per site, thereby inducing a Bloch oscillation. After one full Bloch cycle the gradient is removed and the fraction of atoms ξ in the second band is determined using a band-mapping procedure (Methods). We measure ξ when breaking either IS or TRS, corresponding to the vertical or horizontal axis of the Haldane diagram of Fig. 1b. For broken IS, a gap given by $|\Delta_{AB}|$ opens at both Dirac points, leading to a symmetric decay of ξ around $\Delta_{AB} = 0$, as shown in Fig. 2a. In the case of broken TRS (Fig. 2b), a reduction in transfer versus modulation phase is observed. This signals an opening gap, which is found to be largest for circular modulation, as expected from Eq. (2).

Breaking either IS or TRS gives rise to similar, gapped band structures, which are point-symmetric around quasi-momentum $\mathbf{q} = 0$. However, the resulting topologies of the eigenstates are different and can be characterised by the Berry-curvature $\Omega(\mathbf{q})$. In \mathbf{q} -space, $\Omega(\mathbf{q})$ is analogous to a magnetic field and corresponds to the geometric phase picked up along an infinitesimal loop. When only IS is broken, the Berry-curvature is an odd function of \mathbf{q} , and its sign inverts for opposite Δ_{AB} , see Fig. 2e. The spread of $\Omega(\mathbf{q})$ increases with the size of the gap. Its integral over the first Brillouin-zone (BZ), the Chern number ν , is zero, corresponding to a topologically trivial system. However, with only TRS broken, $\nu = \pm 1$,

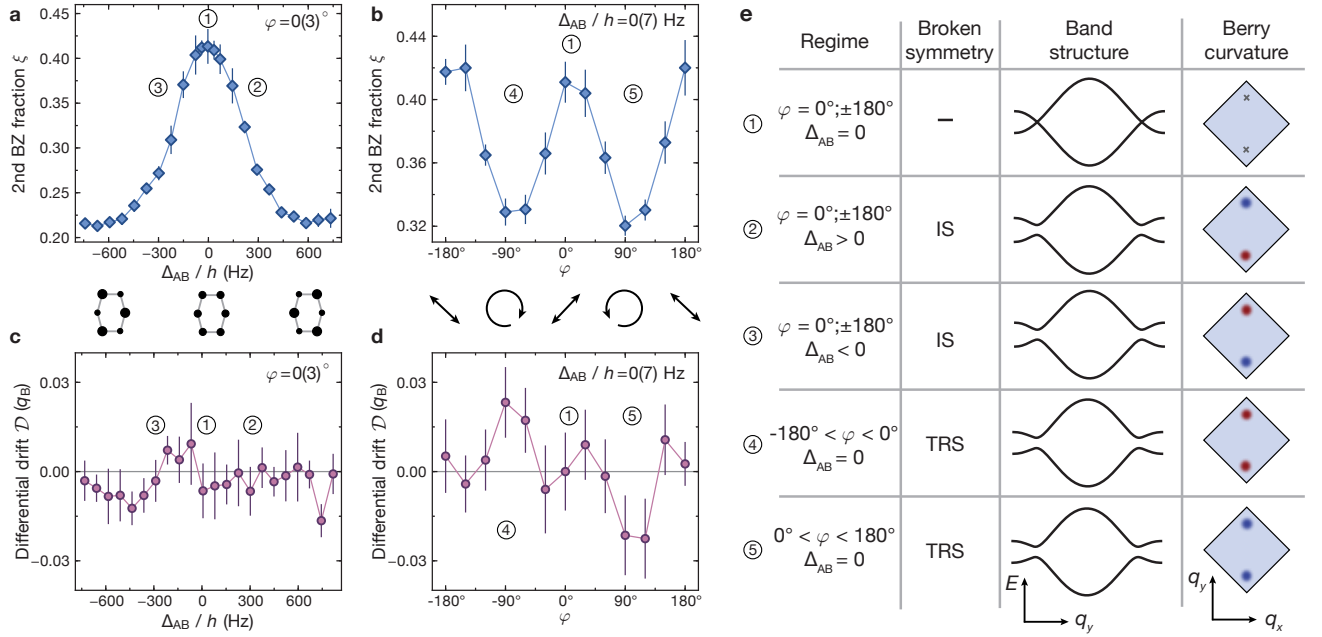


FIG. 2: **Probing gaps and Berry-curvature.** **a+b**, Fraction of atoms in the second band ξ after one Bloch-oscillation in the q_x -direction. We break either IS (**a**) by introducing a sublattice offset Δ_{AB} or TRS (**b**) *via* elliptical modulation (see diagrams below). This corresponds to scanning either of the two axes of the Haldane model. A gap opens at both Dirac points, given by $|\Delta_{AB}|$ or $|\Delta_T^{\max} \sin(\varphi)|$, respectively, thereby reducing ξ . **c+d**, Differential drift \mathcal{D} obtained from Bloch-oscillations in opposite q_y -directions. For broken IS (**c**), opposite Berry-curvatures at the two Dirac points cancel each other, whilst for broken TRS (**d**) the system enters the topological regime, where opposite drifts for $\varphi \gtrless 0$ are expected. Data show mean \pm s.d. of at least 6(**a-c**) or 21(**d**) measurements. **e**, Sketches illustrating gaps and Berry-curvature in different regimes. Red (blue) indicates positive (negative) Berry-curvature.

$\Omega(\mathbf{q})$ is even, and its sign changes when reverting the rotation direction of the lattice modulation.

When atoms move through regions of \mathbf{q} -space with non-zero curvature, they acquire an orthogonal velocity proportional to the applied force and $\Omega(\mathbf{q})$ [23–26]. The underlying harmonic confinement caused by the laser beams in the experiment couples real and momentum-space, leading to a drift in quasi-momentum. We move the atoms along the y -direction such that their trajectories sample the regions where the Berry-curvature is concentrated. We apply a gradient of $\Delta E/h = 114.6(1)$ Hz per site and measure the center of mass of the quasi-momentum distribution in the lowest band after one full Bloch cycle. Subtracting the result for the opposite gradient gives the differential drift \mathcal{D} , which provides more direct access to the Berry-curvature distribution [25]. For individual drifts, which constitute a measurement of the local Berry-curvature, see Supplementary Figs. S14 and S15. When breaking only IS, \mathcal{D} vanishes and is independent of Δ_{AB} , as the Berry-curvature is odd, see Fig. 2c. In contrast, when only TRS is broken, a differential drift is observed for $\varphi = 90^\circ$, which, as expected, is opposite for $\varphi = -90^\circ$ and disappears as the modulation becomes linear, see Fig. 2d and 4c. This is a direct consequence of the Berry-curvature being even, with its sign given by the rotation direction of the lattice modulation.

For these parameters we explore the topological regime of the Haldane model with $\Delta_{AB} = 0$.

Within the Haldane model, the competition of simultaneously broken TRS and IS is of particular interest, as it features a topological transition between a trivial band insulator and a Chern-insulator. In this regime, both the band-structure and Berry-curvature are no longer point-symmetric and the energy gap G_\pm at the two Dirac points is given by

$$G_\pm = |\Delta_{AB} \pm \Delta_T^{\max} \cdot \sin(\varphi)|. \quad (3)$$

On the transition lines the system is gapless with one closed and one gapped Dirac point, $G_+ = 0$ or $G_- = 0$.

We map out the transition by measuring the transfer ξ_\pm for each Dirac point separately, see Fig. 3a. ξ_+ (ξ_-) is the fraction of atoms occupying the upper (lower) half of the second BZ after one Bloch oscillation along the x -direction. The minimum gap for each Dirac point is determined from the point of maximum transfer as a function of Δ_{AB} . When $\varphi = 0^\circ$ we find, as expected for preserved TRS, that the maxima of both ξ_+ and ξ_- coincide, see Fig. 3b. The maxima are shifted in opposite directions for $\varphi = 90^\circ$, showing that the minimum gap for each Dirac point occurs at different values of Δ_{AB} . In between these values the system is in the topologically non-trivial regime. We explore

the position of each maximum for varying φ and find opposite shifts for negative φ as predicted by Eq. (3) using no free parameters, see Fig. 3c.

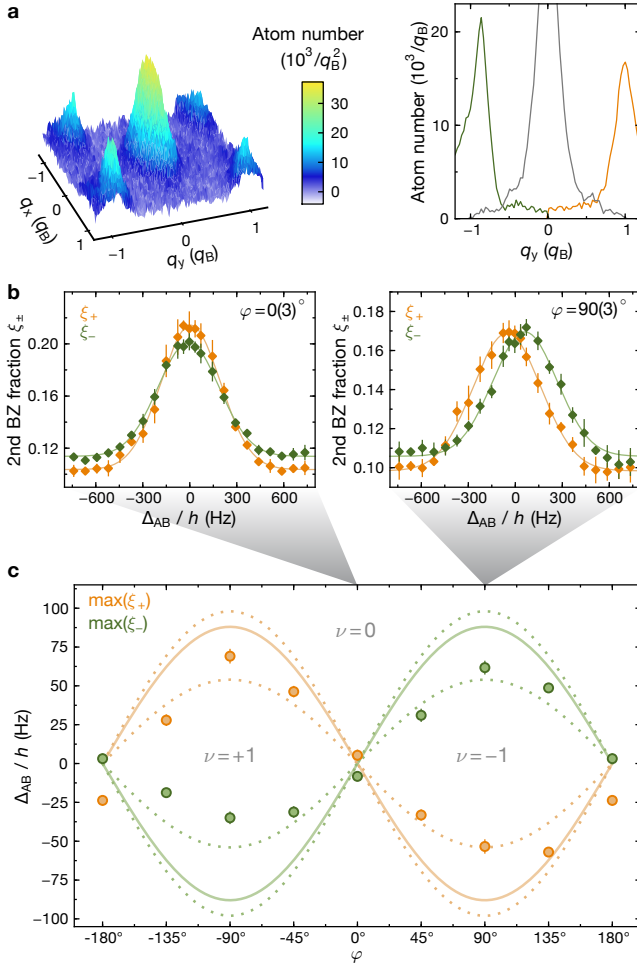


FIG. 3: **Mapping out the transition line.** **a**, Atomic quasi-momentum distribution (averaged over 6 runs) after one Bloch-oscillation for $\varphi = +90^\circ$, $\Delta_{AB}/h = 292(7)$ Hz. A line-sum along q_x shows the atomic density in the first BZ in grey; atoms transferred at the upper (lower) Dirac point are shown in orange (green) throughout. The fraction of atoms in the second BZ differs for $q_y \geq 0$, which is a consequence of simultaneously broken IS and TRS. **b**, Fractions of atoms ξ_{\pm} in each half of the second BZ. For linear modulation (left) the gap vanishes at $\Delta_{AB} = 0$ for both Dirac points, whilst for circular modulation (right) it vanishes at opposite values of Δ_{AB} . Gaussian fits (solid lines) are used to find the maximum transfer, which signals the topological transition. Data are mean \pm s.d. of at least 6 measurements. **c**, Solid lines show the theoretically computed topological transitions, without free parameters. Dotted lines represent the uncertainty of the maximum gap $|\Delta_T^{\max}|/h = 88_{-34}^{+10}$ Hz, originating from the uncertainty of the lattice parameters. Data are the points of maximum transfer for each Dirac point, \pm fit error, obtained from measurements as in **b** for various φ . Between the lines, the system is in the topologically non-trivial regime.

In Figure 4 we show the measured differential drift \mathcal{D} for all topological regimes, allowing for simultaneously broken IS and TRS. Here, we reduce the modulation frequency to 3.75 kHz where the signal-to-noise ratio of \mathcal{D} is larger, but which is less suited for a quantitative comparison of the transfer ξ , as the lattice modulation ramps are expected to be less adiabatic. \mathcal{D} is non-zero only for broken TRS and shows the expected antisymmetry with φ and symmetry with Δ_{AB} . For large Δ_{AB} , deep inside the topologically trivial regime, \mathcal{D} vanishes for all φ . Precursors of the regimes with non-zero Chern number are found to extend well beyond the transition lines. This effect may originate from the large difference of the Berry-curvature distribution and its associated band-structure at the two gapped Dirac points when IS and TRS are simultaneously broken (see Supplementary Figure S13).

Extending our work to interacting systems requires sufficiently low heating. We investigate this with a repulsively interacting spin-mixture in the honeycomb lattice previously used for studying the fermionic Mott insula-

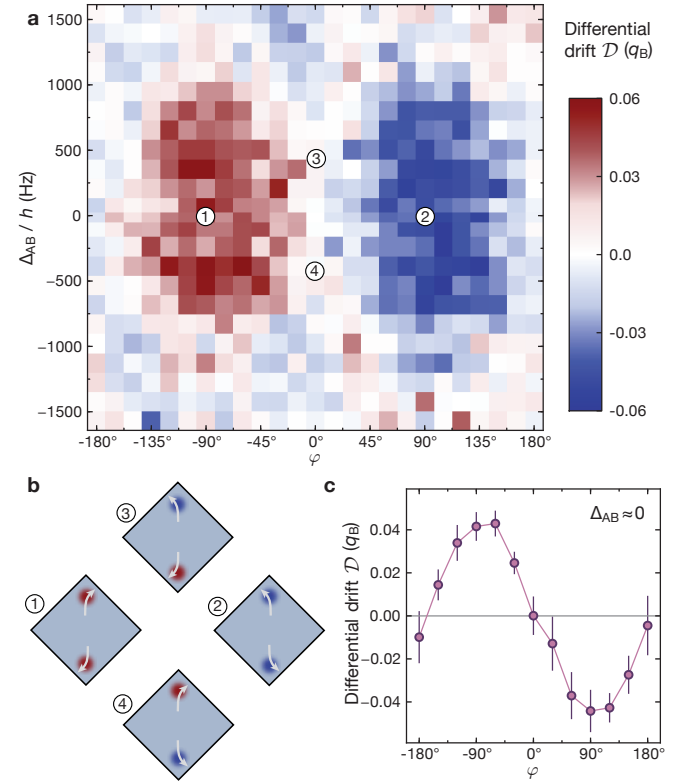


FIG. 4: **Drift measurements.** **a**, Differential drift \mathcal{D} in quasi-momentum. Each pixel corresponds to at least one pair of measurements, where the modulation frequency was set to 3.75 kHz. Data points for $\varphi = \pm 120^\circ$, $\Delta_{AB}/h = 503(7)$ Hz were not recorded and are interpolated. **b**, All topological regimes are explored and the expected momentum-space drifts caused by the Berry-curvature are sketched for selected parameters. **c**, Cut along the $\Delta_{AB}/h = 15(7)$ Hz line. Data show mean \pm s.d. of at least 6 pairs of measurements.

tor [27]. We measure the entropy in the Mott insulating regime by loading into the lattice and reverting the loading procedure (Methods). The entropy increase is only 25% larger than without modulation. This opens the possibility of studying topological models with interactions [28] in a controlled and tunable way. For example, lattice modulation could be used to create topological flat bands, which have been suggested to give rise to interaction-induced fractional Chern-insulators [29, 30]. Furthermore, our approach of periodically modulating the system can be directly extended to engineer Hamiltonians with spin-dependent tunnelling amplitudes and phases. This can be achieved by modulating a magnetic field gradient, which leads to spin-dependent modulation amplitudes owing to the differential Zeeman shift. For example, time-reversal symmetric topological Hamiltonians, such as the Kane-Mele model [3], can be implemented by simultaneously modulating the lattice and magnetic field gradient.

METHODS

Spin polarised Fermi gas. After sympathetic cooling with ^{87}Rb in a magnetic trap, 1×10^6 fermionic ^{40}K atoms are transferred into an optical dipole trap operating at a wavelength of 826 nm. A balanced spin mixture of the $|F, m_F\rangle = |9/2, -9/2\rangle$ and $|9/2, -7/2\rangle$ Zeeman states, where F denotes the hyperfine manifold and m_F the magnetic sub-level, is evaporatively cooled at a magnetic field of 197.6(1) G, in the vicinity of the Feshbach resonance located at 202.1 G. We obtain typical temperatures of $0.2 T_F$, where T_F is the Fermi temperature. The field is subsequently reduced and a magnetic field gradient is used to selectively remove the $|9/2, -7/2\rangle$ component, while levitating the atoms in the $|9/2, -9/2\rangle$ state against gravity.

Honeycomb optical lattice. This polarised Fermi gas is loaded into the optical lattice within 200 ms using an S -shaped intensity ramp, and the dipole trap is subsequently turned off in 100 ms. The lattice potential is given by [8]

$$\begin{aligned} V(x, y, z) = & -V_{\bar{X}} \cos^2(k_L x + \theta/2) - V_X \cos^2(k_L x) \\ & -V_Y \cos^2(k_L y) \\ & -2\alpha \sqrt{V_X V_Y} \cos(k_L x) \cos(k_L y) \cos \varphi_L \\ & -V_{\bar{Z}} \cos^2(k_L z), \end{aligned}$$

where $V_{\bar{X}, X, Y, \bar{Z}}$ are the single-beam lattice depths and $k_L = 2\pi/\lambda$. Gravity points along the negative y -direction. To control the energy offset Δ_{AB} , we vary θ around π by changing the frequency detuning δ between the \bar{X} and the X (which has the same frequency as Y) beams using an acousto-optic modulator (AOM), see Fig. 1c. The phase φ_L is stabilised to $0.0(3)^\circ$ using a

heterodyne interferometer [8], and the visibility of the interference pattern is $\alpha = 0.81(1)$. We minimise the intensity imbalance between the incoming and reflected lattice beams in the $x - y$ plane such that the remaining imbalance between left and right vertical tunnelling is less than 0.3%, as determined from Raman-Nath diffraction on a ^{87}Rb Bose-Einstein condensate. The final lattice depths are set to $V_{\bar{X}, X, Y, \bar{Z}} = [5.0(3), 0.45(2), 2.3(1), 0] E_R$, where $E_R = \hbar^2/2m\lambda^2$, and m denotes the mass of ^{40}K . Using a Wannier function calculation [27], we extract the corresponding tight-binding parameters $t_{0,1,2,3}/\hbar = [-746(81), -527(17), -527(17), -126(7)]$ Hz, for the horizontal, the left and right vertical nearest-neighbour tunnelling links, and the horizontal link across the honeycomb cell, respectively (see Supplementary Material). This results in a bandwidth of $W/\hbar = 3.9(1)$ kHz. The amplitudes for the next-nearest-neighbour tunnel couplings are $t'_{1,2,3}/\hbar = [14, 14, 61]$ Hz and do not affect the gaps and the topological transition line. The nearest-neighbour tunnelling is renormalized in the modulated lattice, which decreases the effective bandwidth to $W_{\text{eff}}/\hbar = 3.3(1)$ kHz. All experiments are carried out in the presence of a weak underlying harmonic confinement with trapping frequencies $\omega_{x,y,z}/2\pi = [14.4(6), 30.2(1), 29.3(3)]$ Hz, which originates from the Gaussian intensity profiles of the red-detuned lattice beams. The lattice depths are calibrated using Raman-Nath diffraction on a ^{87}Rb Bose-Einstein condensate. To determine α , we drive quasi-momentum resolved inter-band transitions for a spin polarised Fermi gas loaded into a checkerboard lattice by periodically modulating the lattice depth and measure the band gap at $\mathbf{q} = 0$.

Modulation of the optical lattice. The two mirrors used for retro-reflecting the lattice beams are mounted on piezo-electric actuators, which allow for a controlled phase shift of the reflected beams with respect to the incoming lattice beams. To fix the geometry of the lattice, the relative phase φ_L of the two orthogonal retro-reflected beams X and Y is actively stabilised to $\varphi_L = 0^\circ$. In order to maintain this phase relation during modulation, the phase of the respective incoming beams is modulated at the same frequency as the piezo-electric actuators using AOMs. In addition, this phase modulation provides a direct calibration of the amplitude and relative phase of the mirror displacement. The calibration is confirmed by measuring both the reduction of tunnelling [10] and the effective atomic mass around $\mathbf{q} = 0$ in a modulated simple cubic lattice.

The modulation is turned on as follows: the atoms are loaded into a lattice with 30% larger single-beam lattice depths than the final values used for the actual measurements. This suppresses resonant transfer of atoms to higher bands. The modulation amplitude is then linearly increased within 20 ms to reach a normalised drive of $K_0 = 0.7778$, where $K_0 = \pi^2 (A/\lambda) (\hbar\omega/E_R)$ with A the amplitude of the motion, $\omega/2\pi$ the modulation

frequency and $\hbar = h/2\pi$. The time-dependence of the lattice position $\mathbf{r}_{\text{lat}}(t)$ is then given by

$$\mathbf{r}_{\text{lat}} = -A \left(\cos(\omega t) \mathbf{e}_x + \cos(\omega t - \varphi) \mathbf{e}_y \right), \quad (4)$$

where \mathbf{e}_x and \mathbf{e}_y denote the real-space unit vectors along the x - and y -direction. When using different modulation frequencies, we keep K_0 constant. We have experimentally verified that the experimental findings are independent of the global phase of the lattice modulation. The lattice depths are then finally reduced in 10 ms to their final values. We have independently verified that the modulation frequency of $\omega/2\pi = 4$ kHz exceeds the combined static bandwidth of the two lowest bands using lattice phase-modulation spectroscopy.

Detection. After one Bloch cycle lasting 9.85 ms (8.72 ms) for x (y) oscillations, the lattice modulation amplitude is linearly lowered to zero within 2 ms. The quasi-momentum distribution of the atoms is then probed using a band mapping technique, where all lattice beams are ramped down within 500 μs , followed by absorption imaging of the atomic distribution after 15 ms of ballistic expansion [8]. The fraction of atoms per band is then determined by integrating the atomic density in the corresponding BZ in the absorption image. Owing to the residual non-adiabaticity of the lattice ramps, 16% (14%) of the atoms are detected in the second band and 21% (8%) in even higher bands after loading the lattice including (not including) the linear ramps of the modulation.

For the drift measurements, the displacement of the atoms with respect to the position before the Bloch oscillation is obtained by calculating the center of mass within the first BZ. The differential drift is then calculated as the difference of the recorded drift for oscillations along the positive and negative q_y -direction. We already observe individual drifts when only breaking IS, which constitutes a measurement of a local Berry-curvature (see Supplementary Material). The drift depends strongly on the size of the energy gap, which can serve as a possible explanation why the precursors of the topological phase extend beyond the phase boundary in Fig. 4.

Effective band-structure calculations. The effective Hamiltonian \hat{H}_{eff} is given by a logarithm of the time-evolution operator for one modulation period. Numerically, we discretise time and \mathbf{q} -space choosing the grid such that a higher resolution does not further change the results. Analytically, we use a Magnus expansion in $1/\omega$. The energy spectrum, Berry-curvature and Chern number are computed from \hat{H}_{eff} using the usual methods employed for static Hamiltonians. By comparing with numerical results and computing higher-order terms we show that the Magnus expansion can be truncated at first order in $1/\omega$ for our parameters, and \hat{H}_{eff} then takes on the form of the Haldane Hamiltonian (Eq. 1).

There, Δ_{AB} is not affected by the modulation com-

pared to the static lattice and t_{ij} are renormalized by a factor of about 0.85 with variations of ± 0.03 , depending on φ and the orientation of the tunnelling. The induced imaginary next-nearest-neighbour tunnelling takes on values of up to $h \times 18$ Hz for the diagonal links and $h \times 5$ Hz for the vertical links. Its value depends only on the modulation amplitude (scaling as a product of two second-order Bessel functions), the frequency (scaling as $1/\omega$), and the product of two nearest-neighbour tunnel couplings which correspond to this next-nearest-neighbour tunnelling. Static real next-nearest neighbour tunnel couplings do not affect other terms in \hat{H}_{eff} and are not required to open a gap, meaning that our approach works equally well in deep optical lattices. The weights w_l determining the gap in Eq. (3) are 3.5 and 2.1 for the vertical and diagonal tunnel couplings respectively, with variations of about ± 0.1 as a function of φ . Detailed derivations, formulae for all terms in the effective Hamiltonian, and comparisons between numerical and analytical approaches can be found in the Supplementary Material.

Lattice modulation heating measurements. In order to measure heating, we prepare about $2.0(2) \times 10^5$ atoms in a balanced spin mixture of the $|F, m_F\rangle = |9/2, -9/2\rangle$ and $|9/2, -5/2\rangle$ Zeeman state. The atoms are loaded into a lattice with final depths $V_{\bar{x},x,y,\bar{z}} = [14.0(4), 0.79(2), 6.45(20), 7.0(2)] E_R$ within 200 ms. This corresponds to a system consisting of coupled isotropic honeycomb layers with a nearest-neighbour tunnelling $t/h = 172(20)$ Hz, as used in previous work [27]. The two lowest bands have a total bandwidth of $h \times 1.0$ kHz, with a gap of $h \times 14$ kHz to the next higher band (excluding the third direction). After turning on the lattice modulation as outlined above (using $\omega/2\pi = 1.08$ kHz and the same K_0 , which opens a gap of about $h \times 44$ Hz at the Dirac points), we reverse the loading procedure and measure the final temperature of the sample. This is compared to a sequence where the lattice is not modulated. From the difference in temperature before loading the lattice and after the procedure, the corresponding entropy increase can be determined. This measurement is performed for an interaction strength of $U/h = 4.18(2)$ kHz ($U/5t = 4.9(6)$), which corresponds to the Mott-insulating regime explored in [27]. We find an entropy increase which is 25% larger when modulating the lattice compared to the situation without modulation. We additionally explore the crossover regime at $U/h = 2.19(5)$ kHz ($U/5t = 2.5(3)$) and find a 40% increase. This possibly originates from the creation of charge excitations for these parameters. Results for additional modulation frequencies and heating rates for longer modulation times are shown in Supplementary Materials.

-
- [1] Haldane, F. D. M. Model for a Quantum Hall Effect without Landau Levels: Condensed-Matter Realization of the "Parity Anomaly". *Phys. Rev. Lett.* **61**, 2015–2018 (1988).
- [2] Chang, C.-Z. *et al.* Experimental observation of the quantum anomalous Hall effect in a magnetic topological insulator. *Science* **340**, 167–170 (2013).
- [3] Kane, C. L. & Mele, E. J. Quantum Spin Hall Effect in Graphene. *Phys. Rev. Lett.* **95**, 226801 (2005).
- [4] König, M. *et al.* Quantum spin Hall insulator state in HgTe quantum wells. *Science* **318**, 766–770 (2007).
- [5] Hsieh, D. *et al.* A topological Dirac insulator in a quantum spin Hall phase. *Nature* **452**, 970–974 (2008).
- [6] Hasan, M. Z. & Kane, C. L. Colloquium: Topological insulators. *Rev. Mod. Phys.* **82**, 3045–3067 (2010).
- [7] Oka, T. & Aoki, H. Photovoltaic Hall effect in graphene. *Phys. Rev. B* **79**, 081406 (2009).
- [8] Tarruell, L., Greif, D., Uehlinger, T., Jotzu, G. & Esslinger, T. Creating, moving and merging Dirac points with a Fermi gas in a tunable honeycomb lattice. *Nature* **483**, 302–305 (2012).
- [9] Dunlap, D. & Kenkre, V. Dynamic localization of a charged particle moving under the influence of an electric field. *Phys. Rev. B* **34**, 3625–3633 (1986).
- [10] Lignier, H. *et al.* Dynamical Control of Matter-Wave Tunneling in Periodic Potentials. *Phys. Rev. Lett.* **99**, 220403 (2007).
- [11] Struck, J. *et al.* Tunable Gauge Potential for Neutral and Spinless Particles in Driven Optical Lattices. *Phys. Rev. Lett.* **108**, 225304 (2012).
- [12] Jiménez-García, K. *et al.* Peierls Substitution in an Engineered Lattice Potential. *Phys. Rev. Lett.* **108**, 225303 (2012).
- [13] Parker, C. V., Ha, L.-C. & Chin, C. Direct observation of effective ferromagnetic domains of cold atoms in a shaken optical lattice. *Nat. Phys.* **9**, 769–774 (2013).
- [14] Zenesini, A., Lignier, H., Ciampini, D., Morsch, O. & Arimondo, E. Coherent Control of Dressed Matter Waves. *Phys. Rev. Lett.* **102**, 100403 (2009).
- [15] Struck, J. *et al.* Quantum simulation of frustrated classical magnetism in triangular optical lattices. *Science* **333**, 996–999 (2011).
- [16] Aidelsburger, M. *et al.* Experimental Realization of Strong Effective Magnetic Fields in an Optical Lattice. *Phys. Rev. Lett.* **107**, 255301 (2011).
- [17] Struck, J. *et al.* Engineering Ising-XY spin-models in a triangular lattice using tunable artificial gauge fields. *Nat. Phys.* **9**, 738–743 (2013).
- [18] Williams, R. A., Al-Assam, S. & Foot, C. J. Observation of Vortex Nucleation in a Rotating Two-Dimensional Lattice of Bose-Einstein Condensates. *Phys. Rev. Lett.* **104**, 050404 (2010).
- [19] Aidelsburger, M. *et al.* Realization of the Hofstadter Hamiltonian with Ultracold Atoms in Optical Lattices. *Phys. Rev. Lett.* **111**, 185301 (2013).
- [20] Miyake, H., Siviloglou, G. A., Kennedy, C. J., Burton, W. C. & Ketterle, W. Realizing the Harper Hamiltonian with Laser-Assisted Tunneling in Optical Lattices. *Phys. Rev. Lett.* **111**, 185302 (2013).
- [21] Rechtsman, M. C. *et al.* Photonic Floquet topological insulators. *Nature* **496**, 196–200 (2013).
- [22] Lim, L.-K., Fuchs, J.-N. & Montambaux, G. Bloch-Zener Oscillations across a Merging Transition of Dirac Points. *Phys. Rev. Lett.* **108**, 175303 (2012).
- [23] Chang, M.-C. & Niu, Q. Berry phase, hyperorbits, and the Hofstadter spectrum. *Phys. Rev. Lett.* **75**, 1348–1351 (1995).
- [24] Dudarev, A. M., Diener, R. B., Carusotto, I. & Niu, Q. Spin-Orbit Coupling and Berry Phase with Ultracold Atoms in 2D Optical Lattices. *Phys. Rev. Lett.* **92**, 153005 (2004).
- [25] Price, H. M. & Cooper, N. R. Mapping the Berry curvature from semiclassical dynamics in optical lattices. *Phys. Rev. A* **85**, 033620 (2012).
- [26] Dauphin, A. & Goldman, N. Extracting the Chern Number from the Dynamics of a Fermi Gas: Implementing a Quantum Hall Bar for Cold Atoms. *Phys. Rev. Lett.* **111**, 135302 (2013).
- [27] Uehlinger, T. *et al.* Artificial Graphene with Tunable Interactions. *Phys. Rev. Lett.* **111**, 185307 (2013).
- [28] Varney, C. N., Sun, K., Rigol, M. & Galitski, V. Interaction effects and quantum phase transitions in topological insulators. *Phys. Rev. B* **82**, 115125 (2010).
- [29] Neupert, T., Santos, L., Chamon, C. & Mudry, C. Fractional Quantum Hall States at Zero Magnetic Field. *Phys. Rev. Lett.* **106**, 236804 (2011).
- [30] Grushin, A. G., Gómez-León, A. & Neupert, T. Floquet Fractional Chern Insulators. *Phys. Rev. Lett.* **112**, 156801 (2014).

Acknowledgements We would like to thank Hideo Aoki for pointing out their proposal in the context of optical lattices and Nigel Cooper, Sebastian Huber, Leticia Tarruell, Lei Wang and Alessandro Zenesini for insightful discussions. We acknowledge SNF, NCCR-QSIT and SQMS (ERC advanced grant) for funding.

Author Contributions The data were measured by G.J., M.M., R.D. and D.G. and analysed by G.J., M.M., R.D., T.U. and D.G. The theoretical framework was developed by G.J. and M.L. All work was supervised by T.E. All authors contributed to planning the experiment, discussions and the preparation of the manuscript.

Author Information The authors declare no competing financial interests. Correspondence and requests for materials should be addressed to T.E. (esslinger@phys.ethz.ch).

Supplementary Material

THEORETICAL FRAMEWORK

In the following we outline the theoretical framework used to obtain effective Hamiltonians for time-modulated optical lattices. In particular, we derive the mapping from an elliptically modulated honeycomb lattice to the Haldane Hamiltonian [S1]. We consider a numerical and analytical approach, compare the results for a wide range of parameters and examine the validity of several approximations for the system studied in the experiment. Some elements of the general framework used there can be found in references [S2–S7], and applications to circularly modulated honeycomb lattices can be found in very recent work [S5, S8, S9].

Effective Hamiltonian of a time-periodic system

The evolution, given by time-evolution operator \hat{U} , of a state obeying a time-periodic Hamiltonian of period T is well captured by an effective Hamiltonian \hat{H}_{eff} over timescales greater than T [S10, S11]. An effective Hamiltonian is defined as, assuming here and henceforth that $\hbar = 1$:

$$\hat{U}(\tau + T, \tau) = \exp(-i\hat{H}_{\text{eff}}^\tau T). \quad (\text{S1})$$

The operator $\hat{H}_{\text{eff}}^\tau$ is known as the Floquet Hamiltonian. By construction, its energy spectrum does not depend on the choice of starting time τ as two time-evolution operators with different starting times τ, τ' are related through a similarity transformation:

$$\begin{aligned} \hat{U}(\tau' + T, \tau') &= \hat{U}(\tau' + T, \tau + T)\hat{U}(\tau + T, \tau)\hat{U}(\tau, \tau') \\ &= \hat{U}(\tau', \tau)\hat{U}(\tau + T, \tau)\hat{U}(\tau', \tau)^{-1} \end{aligned} \quad (\text{S2})$$

and so are two different effective Hamiltonians,

$$\hat{H}_{\text{eff}}^{\tau'} = \hat{U}(\tau', \tau)\hat{H}_{\text{eff}}^\tau\hat{U}(\tau', \tau)^{-1}. \quad (\text{S3})$$

The effective Hamiltonian is proportional to the logarithm of the time-evolution operator over a period T ; therefore its spectrum, known as the quasi-energy spectrum, is only defined modulo $\omega = 2\pi/T$. This logarithm can be evaluated numerically, as detailed in a later section (Eq. (S46) and following). It can alternatively be

expanded as a Magnus series involving multiple integrals and commutators of the time-dependent Hamiltonian: up to first order,

$$\hat{H}_{\text{eff}}^\tau = \hat{H}_{0\omega} + \hat{H}_{1\omega}^\tau + \mathcal{O}\left(\frac{1}{\omega^2}\right) \quad (\text{S4})$$

with

$$\hat{H}_{0\omega} = \frac{1}{T} \int_\tau^{\tau+T} dt \hat{H}(t) \quad (\text{S5})$$

$$\hat{H}_{1\omega}^\tau = -\frac{i}{2T} \int_\tau^{\tau+T} dt \int_\tau^t dt' [\hat{H}(t), \hat{H}(t')]. \quad (\text{S6})$$

Writing $\hat{H}(t)$ as a Fourier series,

$$\hat{H}(t) = \sum_{n=-\infty}^{+\infty} \hat{H}_n e^{in\omega t} \quad (\text{S7})$$

we compute:

$$\hat{H}_{0\omega} = \hat{H}_0 \quad (\text{S8})$$

$$\begin{aligned} \hat{H}_{1\omega}^\tau &= \frac{1}{\omega} \sum_{n=1}^{\infty} \frac{1}{n} \left([\hat{H}_n, \hat{H}_{-n}] \right. \\ &\quad \left. - e^{in\omega\tau} [\hat{H}_n, \hat{H}_0] + e^{-in\omega\tau} [\hat{H}_{-n}, \hat{H}_0] \right). \end{aligned} \quad (\text{S9})$$

To lowest order, the effective Hamiltonian equals the average of the Hamiltonian over one period, while the starting time τ only enters at first order in $1/\omega$ as a phase factor $e^{\pm in\omega\tau}$. The information about the starting phase of the modulation may not be relevant in a number of experimental cases – for example when adiabatically switching on the modulation, as in the experiment we report on. In a different approach [S7, S12], the τ -dependence of $\hat{H}_{\text{eff}}^\tau$ can be absorbed by choosing a particular interaction picture, splitting the evolution into an effective evolution under the Hamiltonian \hat{H}_{eff} and two initial and final “kicks” defined by a T -periodic operator $\hat{K}(\tau)$ which averages to zero over one period:

$$\hat{U}(T + \tau, \tau) = e^{iK(\tau)} e^{-i\hat{H}_{\text{eff}}T} e^{-iK(\tau)}. \quad (\text{S10})$$

The τ -independent effective Hamiltonian can then be expanded up to $1/\omega^2$ as follows:

$$\hat{H}_{\text{eff}} = \hat{H}_{0\omega} + \hat{H}_{1\omega} + \hat{H}_{2\omega} + \mathcal{O}\left(\frac{1}{\omega^3}\right) \quad (\text{S11})$$

$$\text{with } \hat{H}_{0\omega} = \hat{H}_0 \quad (\text{S12})$$

$$\hat{H}_{1\omega} = \frac{1}{\omega} \sum_{n=1}^{\infty} \frac{1}{n} [\hat{H}_n, \hat{H}_{-n}] \quad (\text{S13})$$

$$\begin{aligned} \hat{H}_{2\omega} = & \frac{1}{2\omega^2} \sum_{n=1}^{\infty} \frac{1}{n^2} \left([[\hat{H}_n, \hat{H}_0], \hat{H}_{-n}] + \text{h.c.} \right) \\ & + \frac{1}{3\omega^2} \sum_{n,n'=1}^{\infty} \frac{1}{nn'} \left([\hat{H}_n, [\hat{H}_{n'}, \hat{H}_{-n-n'}]] - 2[\hat{H}_n, [\hat{H}_{-n'}, \hat{H}_{n'-n}]] + \text{h.c.} \right). \end{aligned} \quad (\text{S14})$$

The results presented above are general and valid for any time-periodic Hamiltonian.

Elliptical modulation

We now consider the case of an optical lattice described by a tight-binding model with one orbital per site. The modulation applied in our experiments consists in moving the lattice along a periodic trajectory $\mathbf{r}_{\text{lat}}(t)$, giving rise to an inertial force $\mathbf{F}(t) = -m\ddot{\mathbf{r}}_{\text{lat}}(t)$ exerted on the atoms. In the lattice frame, this amounts to adding a linear, site-dependent potential to the tight-binding Hamiltonian at rest:

$$\hat{H}_{\text{lat}}(t) = \sum_{\langle ij \rangle} t_{ij} \hat{c}_i^\dagger \hat{c}_j + \sum_i (\mathbf{F}(t) \cdot \mathbf{r}_i) \hat{c}_i^\dagger \hat{c}_i \quad (\text{S15})$$

where $\hat{c}_i, \hat{c}_i^\dagger$ denote the annihilation and creation operators on the lattice sites at positions \mathbf{r}_i in the lattice frame, and t_{ij} the tunnelling amplitudes of the static lattice. This additional time-dependent term can in turn be cancelled by shifting the quantum states by the lattice momentum $-\mathbf{q}_{\text{lat}} = -m\dot{\mathbf{r}}_{\text{lat}}(t)$, through the unitary transformation

$$\hat{U}(t) = \exp \left[i \sum_i (-m\dot{\mathbf{r}}_{\text{lat}}(t) \cdot \mathbf{r}_i) \hat{c}_i^\dagger \hat{c}_i \right]. \quad (\text{S16})$$

In the resulting interaction Hamiltonian, this momentum shift is absorbed in complex phase factors of the tunnelling amplitudes,

$$\hat{H}'_{\text{lat}} = \hat{U}^\dagger \hat{H}_{\text{lat}} \hat{U} - i\hat{U}^\dagger \partial_t \hat{U} = \sum_{\langle ij \rangle} e^{i\mathbf{q}_{\text{lat}} \cdot \mathbf{r}_{ij}} t_{ij} \hat{c}_i^\dagger \hat{c}_j \quad (\text{S17})$$

where we define the relative vector between two sites $\mathbf{r}_{ij} = \mathbf{r}_i - \mathbf{r}_j$ and we omit writing the time-dependence of the operators and the lattice momentum for brevity. The elliptical trajectories considered in this paper are created by modulating the lattice position along two or-

thogonal axes $(\mathbf{e}_1, \mathbf{e}_2)$ with equal amplitude A and a relative phase φ ,

$$\mathbf{r}_{\text{lat}}(t) = -A \left(\cos(\omega t) \mathbf{e}_1 + \cos(\omega t - \varphi) \mathbf{e}_2 \right). \quad (\text{S18})$$

Changing φ allows for continuously changing both the aspect ratio of the trajectory (from linear, $\varphi = 0^\circ$ or 180° , to circular, $\varphi = \pm 90^\circ$) and its rotation direction (anticlockwise for $0^\circ < \varphi < 180^\circ$, clockwise for $-180^\circ < \varphi < 0^\circ$). The phase factors in Eq. (S17), which essentially indicate how the lattice velocity $\dot{\mathbf{r}}_{\text{lat}}$ projects onto the lattice bonds \mathbf{r}_{ij} , are therefore sinusoidal functions of time: introducing the modulation parameters

$$\begin{aligned} \rho_{ij} e^{i\phi_{ij}} &= \mathbf{r}_{ij} \cdot \mathbf{e}_1 + \mathbf{r}_{ij} \cdot \mathbf{e}_2 e^{-i\varphi} \\ z_{ij} &= m\omega A \rho_{ij} \end{aligned} \quad (\text{S19})$$

with the convention $\rho_{ij} \geq 0$, the Hamiltonian takes on the general form

$$\hat{H} = \sum_{\langle ij \rangle} e^{iz_{ij} \sin(\omega t + \phi_{ij})} t_{ij} \hat{c}_i^\dagger \hat{c}_j. \quad (\text{S20})$$

Its Fourier-harmonics, as required in Eqs. (S12) to (S14), are obtained using the Jacobi-Anger expansion:

$$\hat{H}_n = \sum_{\langle ij \rangle} J_n(z_{ij}) e^{in\phi_{ij}} t_{ij} \hat{c}_i^\dagger \hat{c}_j \quad (\text{S21})$$

where J_n denotes the n^{th} -order Bessel function of the first kind. Every \hat{H}_n features the same space periodicity and underlying geometry as the tight-binding lattice at rest, with modified tunnelling amplitudes and phases. The Bessel functions of negative order are related to the positive ones through $J_{-n}(z) = (-1)^n J_n(z)$. In the limit of weak modulations ($z_{ij} \ll 1$), we can write $J_n(z_{ij}) = z_{ij}^n / (2^n n!) + \mathcal{O}(z_{ij}^{n+2})$ and limiting the expansion of \hat{H}_{eff} to the lowest orders in n is justified. This no longer holds for stronger modulations, where care has to be taken how the truncation is performed. Note that so far no assumptions about the lattice geometry have been made.

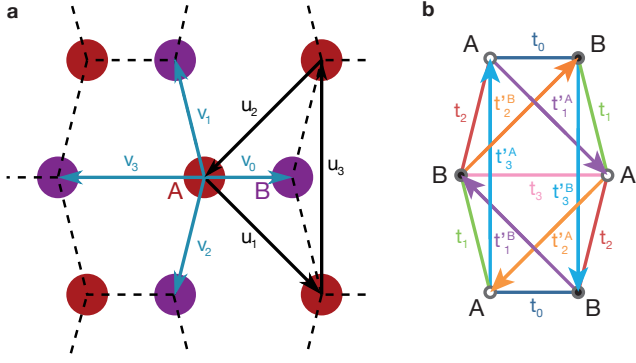


FIG. S1: **a**, Definition of the Bravais lattice vectors $\mathbf{u}_1, \mathbf{u}_2$, intra-sublattice vector \mathbf{u}_3 and the inter-sublattice vectors $\mathbf{v}_0, \mathbf{v}_1, \mathbf{v}_2, \mathbf{v}_3$ for the honeycomb lattices considered in the experiment. **b**, Tunnelling structure. Arrows indicate the definition of phases $\Phi_{j'}$.

Tight-binding model of a bipartite lattice

The honeycomb lattice used in the experiment contains two sites per unit cell, belonging to two different checkerboard sublattices \mathcal{A} and \mathcal{B} , see Fig. S1a. We now allow for an energy difference Δ_{AB} between the two sublattices, which is not affected by the unitary transformation of Eq. (S16), and distinguish the tunnellings t_j connecting \mathcal{A} and \mathcal{B} on the one hand, and the tunnellings t'_{jA} and t'_{jB} within \mathcal{A} and \mathcal{B} on the other hand. The resulting tight-binding Hamiltonian reads:

$$\begin{aligned} \hat{H} = \sum_{\mathbf{u} \in \mathcal{A}} & \left[\frac{\Delta_{AB}}{2} \hat{a}_{\mathbf{u}}^\dagger \hat{a}_{\mathbf{u}} - \frac{\Delta_{AB}}{2} \hat{b}_{\mathbf{u}+\mathbf{v}_0}^\dagger \hat{b}_{\mathbf{u}+\mathbf{v}_0} \right. \\ & + \sum_j (t_j \hat{b}_{\mathbf{u}+\mathbf{v}_j}^\dagger \hat{a}_{\mathbf{u}} + \text{h.c.}) \\ & \left. + \sum_{j'} (t'_{jA} \hat{a}_{\mathbf{u}+\mathbf{u}_{j'}}^\dagger \hat{a}_{\mathbf{u}} + t'_{jB} \hat{b}_{\mathbf{u}+\mathbf{v}_0-\mathbf{u}_{j'}}^\dagger \hat{b}_{\mathbf{u}+\mathbf{v}_0} + \text{h.c.}) \right] \end{aligned} \quad (\text{S22})$$

where the vectors \mathbf{v}_j connect \mathcal{A} - \mathcal{B} site pairs and the vectors $\mathbf{u}_{j'}$ (which include the Bravais lattice vectors) connect \mathcal{A} - \mathcal{A} / \mathcal{B} - \mathcal{B} site pairs. Here, $\hat{a}_{\mathbf{r}}, \hat{a}_{\mathbf{r}}^\dagger$ ($\hat{b}_{\mathbf{r}}, \hat{b}_{\mathbf{r}}^\dagger$) denote the annihilation and creation operators on a site belonging to the \mathcal{A} (\mathcal{B}) sublattice. The Hamiltonian has been chosen such that the complex t'_{jA} and t'_{jB} have their phases defined along the arrows shown in Fig. S1b. Taking the Fourier transform of the annihilation and creation operators on the sublattices,

$$\hat{a}_{\mathbf{q}} = \frac{1}{\sqrt{N}} \sum_{\mathbf{u} \in \mathcal{A}} e^{-i\mathbf{q} \cdot \mathbf{u}} \hat{a}_{\mathbf{u}}, \quad \hat{b}_{\mathbf{q}} = \frac{1}{\sqrt{N}} \sum_{\mathbf{u}' \in \mathcal{B}} e^{-i\mathbf{q} \cdot \mathbf{u}'} \hat{b}_{\mathbf{u}'}$$

the tight-binding Hamiltonian can be rewritten in quasi-momentum space as:

$$\begin{aligned} \hat{H}(\mathbf{q}) &= (\hat{a}_{\mathbf{q}}^\dagger \ \hat{b}_{\mathbf{q}}^\dagger) \begin{pmatrix} h_{AA} & h_{AB}^* \\ h_{AB} & h_{BB} \end{pmatrix} \begin{pmatrix} \hat{a}_{\mathbf{q}} \\ \hat{b}_{\mathbf{q}} \end{pmatrix} \\ &= h_i \hat{I} + h_x \hat{\sigma}_x + h_y \hat{\sigma}_y + h_z \hat{\sigma}_z \end{aligned} \quad (\text{S23})$$

where we define the operators $\hat{O} = (\hat{a}_{\mathbf{q}}^\dagger, \hat{b}_{\mathbf{q}}^\dagger) O(\hat{a}_{\mathbf{q}}, \hat{b}_{\mathbf{q}})^T$ acting on the space spanned by the Bloch waves residing on the two sublattices $\hat{a}_{\mathbf{q}}^\dagger |0\rangle$ and $\hat{b}_{\mathbf{q}}^\dagger |0\rangle$, with I the 2×2 identity matrix and $\sigma_{x,y,z}$ the Pauli matrices satisfying the commutation relations $[\sigma_\alpha, \sigma_\beta] = 2i\epsilon_{\alpha\beta\gamma}\sigma_\gamma$. The coefficients $h_{i,x,y,z}$ are expressed as:

$$h_i = \sum_{j'} \text{Re}(t'_{jA} + t'_{jB}) \cos(\mathbf{q} \cdot \mathbf{u}_{j'}) + \text{Im}(t'_{jA} - t'_{jB}) \sin(\mathbf{q} \cdot \mathbf{u}_{j'}) \quad (\text{S24})$$

$$h_x = \text{Re} \left(\sum_j t_j e^{i\mathbf{q} \cdot \mathbf{v}_j} \right), \quad h_y = \text{Im} \left(\sum_j t_j e^{i\mathbf{q} \cdot \mathbf{v}_j} \right) \quad (\text{S25})$$

$$h_z = \frac{\Delta_{AB}}{2} + \sum_{j'} \text{Re}(t'_{jA} - t'_{jB}) \cos(\mathbf{q} \cdot \mathbf{u}_{j'}) + \text{Im}(t'_{jA} + t'_{jB}) \sin(\mathbf{q} \cdot \mathbf{u}_{j'}) \quad (\text{S26})$$

The energies of the associated energy bands are

$$\epsilon_{\pm}(\mathbf{q}) = h_i \pm \sqrt{h_x^2 + h_y^2 + h_z^2}. \quad (\text{S27})$$

The Dirac points are located at the quasi-momenta \mathbf{q}_D where $h_x(\mathbf{q}_D) = h_y(\mathbf{q}_D) = 0$, which is a necessary condition for band degeneracy, $\epsilon_+(\mathbf{q}_D) = \epsilon_-(\mathbf{q}_D)$. If all tun-

nel couplings t_j are real, every Dirac point \mathbf{q}_D is paired with another one at opposite quasi-momentum $-\mathbf{q}_D$, as $h_x(-\mathbf{q}_D) = h_x(\mathbf{q}_D)$ and $h_y(-\mathbf{q}_D) = -h_y(\mathbf{q}_D)$. In the case where $t_{j'}^A = t_{j'}^B = t_{j'} e^{i\Phi_{j'}}$ for all j' , the gaps at two opposite Dirac points $\pm\mathbf{q}_D$ are given by

$$G_{\pm} = \epsilon_+(\pm\mathbf{q}_D) - \epsilon_-(\pm\mathbf{q}_D) = |\Delta_{AB} \pm \Delta_T|. \quad (\text{S28})$$

$|\Delta_T|$ is the gap induced by the complex tunnellings when inversion symmetry is preserved ($\Delta_{AB} = 0$),

$$\Delta_T = - \sum_{j'} w_{j'} t_{j'}' \sin(\Phi_{j'}). \quad (\text{S29})$$

It is the sum of the imaginary parts of the complex amplitudes $t_{j'}' e^{i\Phi_{j'}}$ weighted by $w_{j'} = -4 \sin(\mathbf{q}_D \cdot \mathbf{u}_{j'})$. The weights are positive for the lattice used in our experiment, but can also be negative. Their norms are sensitive to the position of the Dirac points, given by the identity $\sum_j t_j e^{\mathbf{q}_D \cdot \mathbf{v}_j} = 0$, and therefore depend on the

inter-sublattice tunnel couplings t_j on the one hand, and the vectors \mathbf{v}_j setting the geometry of the lattice on the other hand.

Analytical effective Hamiltonian

We now derive an analytical expression of the effective Hamiltonian of the lattice under elliptical modulation in the approach exposed earlier. We assume that the next-nearest couplings of the static lattice are real and show $\mathcal{A} - \mathcal{B}$ symmetry, $t_{j'}^A = t_{j'}^B = t_{j'}'$. This symmetry may be broken experimentally but the size of this effect is negligible for the lattices considered in this work. The harmonics of the modulated Hamiltonian, whose tunnel couplings are modified according to Eq. (S21), can be transformed in momentum space \mathbf{q} as $\hat{H}_n = h_{ni} \hat{I} + h_{nx} \hat{\sigma}_x + h_{ny} \hat{\sigma}_y + h_{nz} \hat{\sigma}_z$, with

$$h_{ni} = \sum_{j'} 2J_n(z_{j'}) t_{j'}' \cos(\mathbf{q} \cdot \mathbf{u}_{j'}) \quad (\text{S30})$$

$$h_{nx} = \sum_j \frac{1}{2} [e^{i\mathbf{q} \cdot \mathbf{v}_j} + (-1)^n e^{-i\mathbf{q} \cdot \mathbf{v}_j}] J_n(z_j) e^{in\phi_j} t_j \quad (\text{S31})$$

$$h_{ny} = \sum_j \frac{1}{2i} [e^{i\mathbf{q} \cdot \mathbf{v}_j} - (-1)^n e^{-i\mathbf{q} \cdot \mathbf{v}_j}] J_n(z_j) e^{in\phi_j} t_j \quad (\text{S32})$$

$$h_{nz} = \frac{\Delta_{AB}}{2} \delta_n. \quad (\text{S33})$$

Note that h_{nx} and h_{ny} are complex numbers, which accounts for the fact that $\hat{H}_n = \hat{H}_{-n}^\dagger$ is in general not

Hermitian. δ_n denotes the Kronecker delta. Inserting these expressions into Eqs. (S12) to (S14) results in

$$\hat{H}_{0\omega} = \sum_{j'} 2t_{0,j'}' \cos(\mathbf{q} \cdot \mathbf{u}_{j'}) \hat{I} + \sum_j t_{0,j} [\cos(\mathbf{q} \cdot \mathbf{v}_j) \hat{\sigma}_x + \sin(\mathbf{q} \cdot \mathbf{v}_j) \hat{\sigma}_y] + \frac{\Delta_{AB}}{2} \hat{\sigma}_z \quad (\text{S34})$$

$$\hat{H}_{1\omega} = \sum_{j_1 > j_2} 2t_{1,j_1 j_2} \sin(\mathbf{q} \cdot \mathbf{v}_{j_1 j_2}) \hat{\sigma}_z \quad (\text{S35})$$

$$\begin{aligned} \hat{H}_{2\omega} = & \sum_{j_1, j_2, j_3} t_{2,j_1 j_2 j_3} [\cos \mathbf{q} \cdot (\mathbf{v}_{j_1 j_2} - \mathbf{v}_{j_3}) \hat{\sigma}_x + \sin \mathbf{q} \cdot (\mathbf{v}_{j_1 j_2} - \mathbf{v}_{j_3}) \hat{\sigma}_y] \\ & + \sum_{j_1, j_2, j_3} t_{2,j_1 j_2 j_3} [\cos \mathbf{q} \cdot (-\mathbf{v}_{j_1 j_2} - \mathbf{v}_{j_3}) \hat{\sigma}_x + \sin \mathbf{q} \cdot (-\mathbf{v}_{j_1 j_2} - \mathbf{v}_{j_3}) \hat{\sigma}_y] + \sum_{j_1 > j_2} 2t_{2,j_1 j_2} \cos(\mathbf{q} \cdot \mathbf{v}_{j_1 j_2}) \hat{\sigma}_z \end{aligned} \quad (\text{S36})$$

$$t_{0,j} = J_0(z_j) t_j \quad t'_{0,j'} = J_0(z_{j'}) t'_{j'}, \quad (\text{S37})$$

$$t_{1,j_1 j_2} = \frac{2t_{j_1} t_{j_2}}{\omega} \sum_{n=1}^{\infty} \frac{(-1)^n}{n} \sin[n(\phi_{j_1} - \phi_{j_2})] J_n(z_{j_1}) J_n(z_{j_2}) \quad (\text{S38})$$

$$t_{2,j_1 j_2} = \frac{2\Delta_{AB} t_{j_1} t_{j_2}}{\omega^2} \sum_{n=1}^{\infty} \frac{1}{n^2} \cos[n(\phi_{j_1} - \phi_{j_2})] J_n(z_{j_1}) J_n(z_{j_2}) \quad (\text{S39})$$

$$t_{2,j_1 j_2 j_3} = \frac{2t_{j_1} t_{j_2} t_{j_3}}{\omega^2} \left[\sum_{n \text{ odd}} \frac{1}{n^2} \cos[n(\phi_{j_1} - \phi_{j_2})] J_n(z_{j_1}) J_n(z_{j_2}) J_0(z_{j_3}) - \sum_{n \text{ even}} \frac{i}{n^2} \sin[n(\phi_{j_1} - \phi_{j_2})] J_n(z_{j_1}) J_n(z_{j_2}) J_0(z_{j_3}) \right] \quad (\text{S40})$$

At the lowest order, $\hat{H}_{0\omega}$, all inter-sublattice tunnel couplings $t_{0,j}$ and intra-sublattice tunnel couplings $t_{0,j'}$ are renormalized according to the zeroth order Bessel function $J_0(z_j)$ while the sublattice offset Δ_{AB} remains unaffected.

The first-order term $\hat{H}_{1\omega}$ adds a purely imaginary part $it'_{1,j_1 j_2}$ (*cf.* Equation (S26)) to the preexisting next-nearest neighbour (NNN) couplings, now indexed by pairs of sites (j_1, j_2) connected by the vector $\mathbf{v}_{j_1 j_2} = \mathbf{v}_{j_1} - \mathbf{v}_{j_2}$. Under this form, the new tunnellings may be interpreted as a succession of two virtual tunnel processes with amplitudes $J_0(z_{j_1}) t_{j_1}$ and $J_0(z_{j_2}) t_{j_2}$. Note that the size of this induced NNN tunnelling depends only on the size of the static NN tunnelling, meaning that the scheme does not require shallow lattices.

The second order term $\hat{H}_{2\omega}$ leads to new complex NN and NNNN tunnellings $t_{2,j_1 j_2}$, as well as a real $\mathcal{A} - \mathcal{B}$ imbalance $\pm t_{2,j_1 j_2 j_3}$ of the NNN tunnellings if $\Delta_{AB} \neq 0$. The static next-nearest-neighbour couplings $t'_{j'}$ do not appear anywhere but in the zeroth order term $t_{0,j'}$, and

therefore do not affect the energy-splitting between the two bands.

In general, prefactors to the identity matrix in Eq. (S23) will not contribute to higher-order terms in the effective Hamiltonian, as the commutators $[I, \sigma_\alpha]$ in Eqs. (S9), (S13) and (S14) vanish. Importantly, this means that the next-nearest-neighbour tunnellings of the static lattice do not affect the position of the topological transition lines. In absence of interactions, the presence of the higher-order terms crucially relies on the presence of two bands or more for the commutators in Eqs. (S9), (S13) and (S14) not to be zero. The higher-order terms hence vanish when considering non-interacting atoms on lattices with a single orbital per unit cell.

For completeness, we also provide the τ -dependent term at $1/\omega$ order, although it is not used, as explained above. The expression may however be relevant for experiments where a modulation is suddenly switched on. Denoting the additional term containing the commutators $[\hat{H}_{\pm n}, \hat{H}_0]$ in Eq. (S9) as $\hat{H}_{1\omega}^\tau$, we find

$$\hat{H}_{1\omega}^\tau = \sum_j t_{1,j}^\tau [\cos(\mathbf{q} \cdot \mathbf{v}_j) \hat{\sigma}_x + \sin(\mathbf{q} \cdot \mathbf{v}_j) \hat{\sigma}_y] + \left\{ \frac{\Delta_1^\tau}{2} + \sum_{j_1 > j_2} \left[2t_{1,j_1 j_2}^{\tau \text{ Re}} \cos(\mathbf{q} \cdot \mathbf{v}_{j_1 j_2}) + 2t_{1,j_1 j_2}^{\tau \text{ Im}} \sin(\mathbf{q} \cdot \mathbf{v}_{j_1 j_2}) \right] \right\} \hat{\sigma}_z \quad (\text{S41})$$

$$t_{1,j}^\tau = - \sum_{n \text{ odd}} \frac{2\Delta_{AB} t_j}{n\omega} J_n(z_j) \cos[n(\phi_j + \omega\tau)] - i \sum_{n \text{ even}} \frac{2\Delta_{AB} t_j}{n\omega} J_n(z_j) \cos[n(\phi_j + \omega\tau)] \quad (\text{S42})$$

$$\Delta_1^\tau = \sum_{n \text{ odd}} \sum_j \frac{2t_j^2}{n\omega} J_n(z_j) J_0(z_j) \cos[n(\phi_j + \omega\tau)] \quad (\text{S43})$$

$$t_{1,j_1 j_2}^{\tau \text{ Re}} = \sum_{n \text{ odd}} \frac{2t_{j_1} t_{j_2}}{n\omega} \left[J_n(z_{j_1}) J_0(z_{j_2}) \cos[n(\phi_{j_1} + \omega\tau)] + J_0(z_{j_1}) J_n(z_{j_2}) \cos[n(\phi_{j_2} + \omega\tau)] \right] \quad (\text{S44})$$

$$t_{1,j_1 j_2}^{\tau \text{ Im}} = - \sum_{n \text{ even}} \frac{2t_{j_1} t_{j_2}}{n\omega} \left[J_n(z_{j_1}) J_0(z_{j_2}) \sin[n(\phi_{j_1} + \omega\tau)] - J_0(z_{j_1}) J_n(z_{j_2}) \sin[n(\phi_{j_2} + \omega\tau)] \right] \quad (\text{S45})$$

In addition to (S34) and (S35), the effective τ -dependent Hamiltonian features complex NN tunnel couplings $t_{1,j}^\tau$,

a sublattice offset Δ_1^τ and complex NNN tunnel couplings $t_{1,j_1 j_2}^{\tau \text{ Re}} + it_{1,j_1 j_2}^{\tau \text{ Im}}$.

Numerical effective Hamiltonian

For all numerical calculations, $\hat{H}(t)$ is approximated by an operator $\hat{H}(t_i)$ that is piece-wise constant on N consecutive time intervals $[t_i, t_{i+1}[$, where $t_i = iT/N$, $i = 0 \dots N-1$. This enables us to rewrite the time-evolution operator over $[0, T[$ as the product of N shorter time-evolution operators:

$$\hat{U}(T, 0) = \prod_{i=0}^{N-1} U(t_{i+1}, t_i) = \prod_{i=0}^{N-1} e^{-i\hat{H}(t_i)T/N}. \quad (\text{S46})$$

$\hat{H}(t_i)$ is evaluated for every \mathbf{q} separately according to Eq. (S20). The effective Hamiltonian \hat{H}_{eff}^0 is then computed from Eq. (S1),

$$\hat{H}_{\text{eff}}^0 = \frac{i}{T} \log \hat{U}(T, 0). \quad (\text{S47})$$

Its eigenvectors $|u_{\mathbf{q}}^{\pm}\rangle$ and energies $\epsilon(\mathbf{q})$ are further used to compute the Berry curvature for the lowest energy band [S13]:

$$\Omega(\mathbf{q}) = 2 \text{Im} \left[\frac{\langle u_{\mathbf{q}}^- | \partial_{q_1} \hat{H}_{\text{eff}}^0(\mathbf{q}) | u_{\mathbf{q}}^+ \rangle \langle u_{\mathbf{q}}^+ | \partial_{q_2} \hat{H}_{\text{eff}}^0(\mathbf{q}) | u_{\mathbf{q}}^- \rangle}{(\epsilon_+(\mathbf{q}) - \epsilon_-(\mathbf{q}))^2} \right] \quad (\text{S48})$$

approximating the partial derivatives along the axes of the Brillouin zone by their first order finite-difference expressions. The Chern number is obtained by integrating the Berry curvature over the entire Brillouin zone:

$$\nu = \frac{1}{2\pi} \int_{\mathbf{q} \in \text{BZ}} d^2\mathbf{q} \Omega(\mathbf{q}), \quad (\text{S49})$$

where the integral is replaced by a sum over a discrete grid. The grid spacing and number of time steps are always chosen such that a higher resolution does not change the results we obtain any further. The numerical calculations do include τ -dependent terms, and we have verified that changing τ does not affect the energy spectrum, as expected from Eq. (S3).

With this numerical approach the effect of other types of modulation can also be computed. For example, we verify that a cyclic modulation of the tunnelling amplitudes can also be used to create topological bands, as shown in [S14].

Results for an ideal brickwall lattice

We first consider an idealised version of the lattice realised in the experiment, which exhibits nearly all features of the realistic lattice when applying elliptical modulation: the balanced brickwall lattice, whose horizontal and vertical bonds are all of equal length ($|\mathbf{v}_0| = |\mathbf{v}_1| = |\mathbf{v}_2| = \lambda/2$), at square angle, and which only includes

the three main nearest-neighbour tunnel couplings, with equal tunnelling amplitudes ($t_0 = t_1 = t_2 = t$ and $t_3 = t'_1 = t'_2 = t'_3 = 0$). In the presence of inversion symmetry, $\Delta_{\text{AB}} = 0$, an elliptical modulation opens an equal gap at both Dirac points, located at quasi-momenta $\pm \mathbf{q}_D = \mp 4\pi/(3\lambda^2) \mathbf{u}_1 \mp 4\pi/(3\lambda^2) \mathbf{u}_2$. This fixes the weights present in Eq. (S29) to $w_1 = w_2 = w_3 = 2\sqrt{3}$. Since \mathbf{v}_0 is horizontal and $\mathbf{v}_1, \mathbf{v}_2$ are vertical, the modulation amplitudes z_{ij} of the NN bonds (as defined in Eq. (S19)) are always $K_0 = \pi^2 (A/\lambda) (\hbar\omega/E_R) = m\omega A\lambda/2 = 0.7778$. Therefore the effective nearest-neighbour tunnellings are

$$t_0^{\text{eff}} = t_1^{\text{eff}} = t_2^{\text{eff}} = tJ_0(K_0), \quad (\text{S50})$$

independent of φ . The associated modulation phases are exactly $\phi_0 = 0$, $\phi_1 = -\varphi$ and $\phi_2 = \pi - \varphi$, which allows for expressing the new complex NNN tunnelling (S38) as

$$t_1^{\text{eff}} = i \frac{2t^2}{\omega} \sum_{n=1}^{\infty} \frac{(-1)^n}{n} \sin(n\varphi) [J_n(K_0)]^2 \quad (\text{S51})$$

$$t_2^{\text{eff}} = -i \frac{2t^2}{\omega} \sum_{n=1}^{\infty} \frac{1}{n} \sin(n\varphi) [J_n(K_0)]^2 \quad (\text{S52})$$

$$t_3^{\text{eff}} = 0. \quad (\text{S53})$$

Consequently, the energy offset caused by breaking TRS reads

$$\begin{aligned} \Delta_T &= \frac{8\sqrt{3}t^2}{\omega} \sum_{n \text{ odd}} \frac{1}{n} \sin(n\varphi) [J_n(K_0)]^2 \\ &\approx \Delta_T^{\text{max}} \sin(\varphi). \end{aligned} \quad (\text{S54})$$

The approximation corresponds to keeping only the $n = 1$ term of the sum, with $\Delta_T^{\text{max}} = 8\sqrt{3}[tJ_1(K_0)]^2/\omega$. For $K_0 = 0.7778$ (as used in the experiment), this approximation deviates by less than 0.1% from the asymptotic value of the maximum gap obtained for $n \rightarrow \infty$.

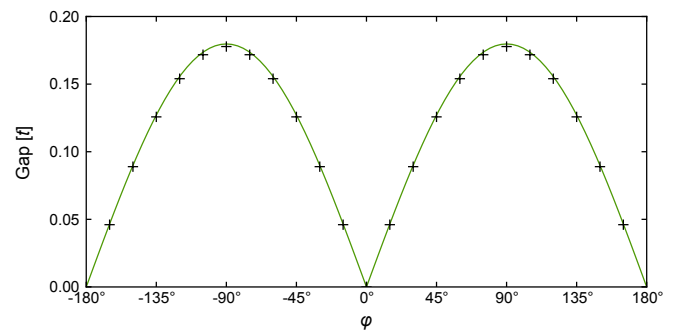


FIG. S2: Analytically and numerically computed gap versus relative phase φ between horizontal and vertical modulation, for an ideal brickwall lattice and $\omega = 10t$. $K_0 = \pi^2 (A/\lambda) (\hbar\omega/E_R) = m\omega A\lambda/2 = 0.7778$ is the dimensionless parameter for the modulation amplitude. Here and in the following figures, points (lines) indicate the numerical (analytical) results.

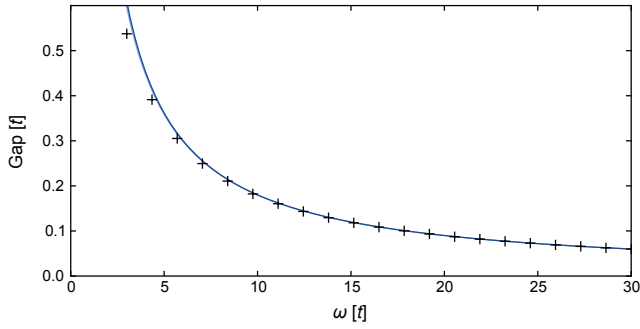


FIG. S3: Absolute gap versus modulation frequency ω , for circular modulation $\varphi = \pm 90^\circ$, $K_0 = 0.7778$. The dark (light) blue line shows the analytical results truncated at first (second) order in $1/\omega$. The two lines are almost identical.

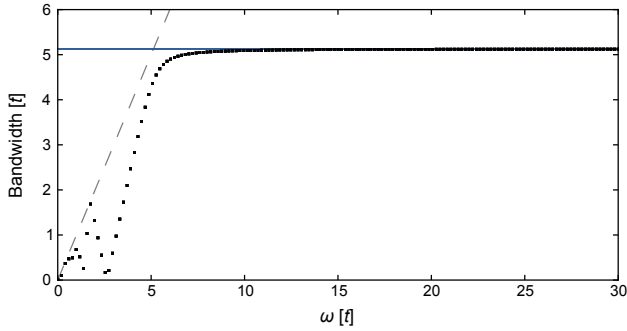


FIG. S4: Bandwidth (defined as the energy splitting at $\mathbf{q} = 0$) versus modulation frequency ω , for circular modulation $\varphi = \pm 90^\circ$, $K_0 = 0.7778$. The dashed grey line indicates the identity line $f(\omega) = \omega$ which sets the maximum possible bandwidth of the quasi-energy spectrum.

Fig. S2 shows the gap as a function of φ computed through both numerical and analytic methods; they show overall excellent agreement with a relative difference of approximately 1%.

Figs. S3 and S4 show the frequency dependence of the gap and the bandwidth of the effective quasi-energy band-structure. Whereas the bandwidth remains close to its static value renormalized by the zeroth-order Bessel function ($6tJ_0(K_0) \approx 5.13t$ with $K_0 = 0.7778$), the gap increases as the modulation frequency ω decreases and goes like $1/\omega$ for $\omega \gg t$. We find only minor corrections owing to the $1/\omega^2$ term of the analytic expansion, meaning that a truncation to 1st order in $1/\omega$ is acceptable for our parameters. Deviations from the numerical calculations start to appear for frequencies below the static bandwidth $6t$. The induced gap remains considerable even for the highest frequencies that would realistically be employed in an experiment. Truncating the effective Hamiltonian at 0th order in $1/\omega$ is therefore not a valid approximation for the honeycomb lattice.

The gap is a non-monotonic function of the modulation amplitude K_0 . It is well matched by the analytic expansion

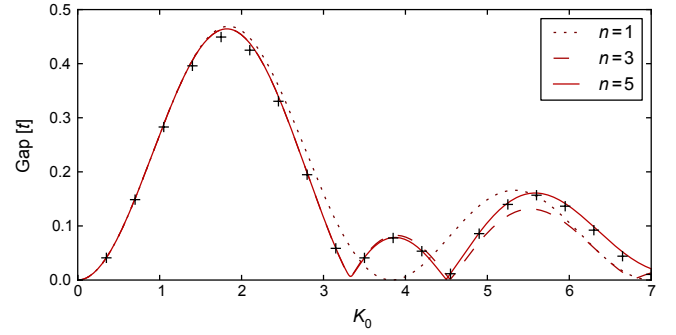


FIG. S5: Absolute gap versus modulation amplitude K_0 , for circular modulation $\varphi = \pm 90^\circ$, $\omega = 10t$. The analytic line is plotted at second order in $1/\omega$ and increasing number n of the harmonics in the time-dependent Hamiltonian expansion. The gap changes sign around $K_0 = 4$

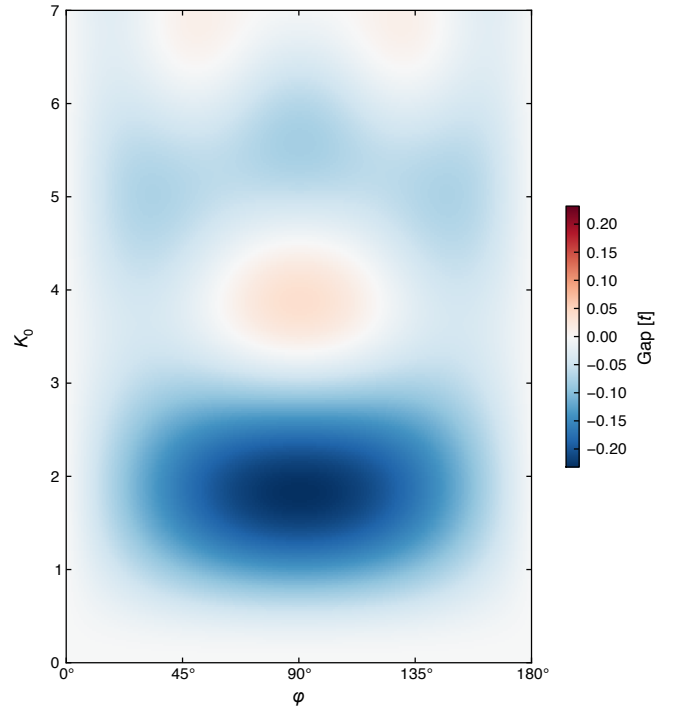


FIG. S6: Analytically computed gap versus relative phase φ and modulation amplitude K_0 at $\omega = 10t$. Red indicates the $\nu = 1$ phase, blue the $\nu = -1$ phase.

sion up to $n = 1$ for amplitudes below $K_0 \approx 2$, whilst for amplitudes up to $K_0 \approx 7$ expanding to at least $n = 5$ is necessary (Fig. S5). Strikingly, the sign of the gap (and therefore the Chern number ν) alternates for increasing K_0 (the first inversion occurs between $K_0 = 3.3$ and 4.5), which is also *not* predicted by the first order theory. The general phase diagram in (φ, K_0) space is drawn in Fig. S6, and shows that, for certain large values of K_0 , the $\nu = +1$ phase becomes accessible for positive φ .

With a preexisting sublattice offset Δ_{AB} , the gaps at the two Dirac points differ as soon as the modulation

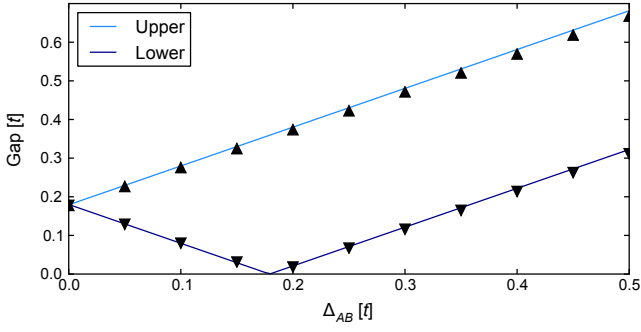


FIG. S7: Absolute gap for the two Dirac points vs. sublattice offset Δ_{AB} with $\varphi = 90^\circ$, $\omega = 10t$, $K_0 = 0.7778$. The single vanishing gap signals the topological transition.

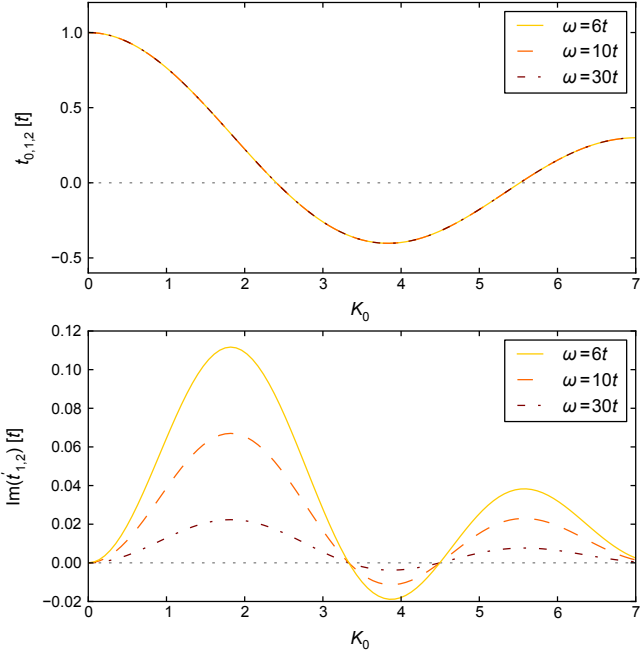


FIG. S8: Tunnelling versus modulation amplitude K_0 , for circular modulation $\varphi = 90^\circ$ at frequencies $\omega = 30t, 10t, 6t$. The contribution from the $1/\omega^2$ term to the tunnellings between \mathcal{A} and \mathcal{B} sublattices is below $10^{-3}t$ at $\omega = 6t$.

is switched on, $K_0 > 0$, as shown in Fig. S7. One of them closes as soon as $\Delta_{AB} = \Delta_T$, as expected from the Haldane model (see also Eq. (3) of the main text).

While the effective energy bands do not depend on any particular choice of the modulation starting time τ , the tunnel couplings do when using the numerical approach (Eqs. (S42) to (S45)). Fig. S8 reports on the tunnellings as computed analytically through Eqs. (S37) to (S40), where the dependence is explicitly absent. As stated in Eq. (S50) all NN tunnellings are evenly renormalized according to the zero-order Bessel function (Fig. S8), independent of ω . To a good approximation, the t'_1, t'_2 tunnellings are purely imaginary and display the ω, K_0 dependence of the gap highlighted in Figs. S3 and S5.

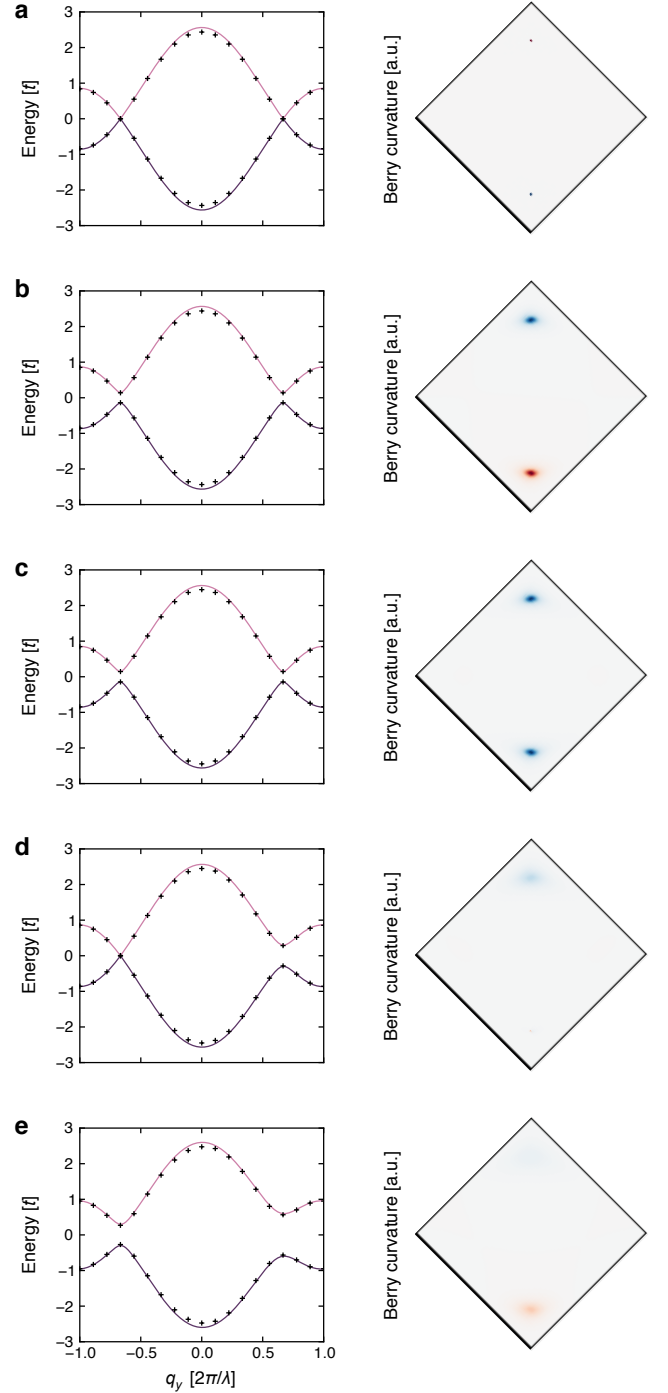


FIG. S9: Cut of the energy bands along the vertical line $q_x = 0$ and Berry curvature of the modulated ideal brickwall lattice for $\omega = 6t$, $K_0 = 0.778$ and

- a. $\varphi = 0$, $\Delta_{AB} = 0$ (IS and TRS not broken);
- b. $\varphi = 0$, $\Delta_{AB} = |\Delta_T^{\max}| \approx 0.30t$ (trivial phase, $\nu = 0$);
- c. $\varphi = 90^\circ$, $\Delta_{AB} = 0$ (non-trivial phase, $\nu = -1$);
- d. $\varphi = 90^\circ$, $\Delta_{AB} = \Delta_T^{\max}$ (topological transition);
- e. $\varphi = 90^\circ$, $\Delta_{AB} = 3\Delta_T^{\max}$ (trivial phase, $\nu = 0$). Note that in e, the gap induced by IS is larger than the gap related to broken TRS, but the latter clearly influences the band-structure and Berry-curvature.

	Static	$\varphi = 0^\circ$	$\varphi = 180^\circ$	$\varphi = \pm 90^\circ$
t_0	-746	-662	-662	-662
t_1	-527	-467	-431	-449
t_2	-527	-431	-467	-449
t_3	-126	-103	-103	-103
t'_1	14	14	7	$10 \mp 18i$
t'_2	14	7	14	$10 \mp 18i$
t'_3	61	29	29	$29 \mp 5i$

TABLE S1: Parameters of the static lattice used in the experiment (as frequencies t/h in units of Hz), obtained through an *ab initio* computation of the Wannier functions [S15], along with their modified values in presence of linear or circular modulation ($\omega = 2\pi \times 4000$ Hz, $K_0 = 0.7778$), calculated analytically. When going from one kind of linear modulation to the orthogonal one ($\varphi = 0^\circ \leftrightarrow 180^\circ$), tunnelling energies are swapped according to a $x \mapsto -x$ reflection. Reverting the modulation from clockwise ($\varphi = -90^\circ$) to anticlockwise ($\varphi = +90^\circ$) replaces the next-nearest-neighbour couplings by their complex conjugates. Furthermore, $|\mathbf{v}_0| = 0.438 \lambda$

In Figure S9 numerical and analytical results for the entire band-structure are shown for exemplary parameters, as well as analytically computed Berry-curvature distributions. Additionally, we confirm that the numerically computed Berry-curvature results in Chern numbers of 0.0 and ± 1.0 where expected. Overall we see that the analytical solution, truncated at 1st order in $1/\omega$ provides reliable results for all experimentally relevant regimes.

Results for the experimental honeycomb lattice

Compared to the idealised case treated above, in the lattice realised in the experiment the NN tunnelling are not all equal (and $t_3 \neq 0$), meaning that the induced tunnel couplings and the weights contributing to the gap are also different. Furthermore, the static real NNN tunnel couplings are not zero, which affects the shape of the band-structure, but not the energy difference between the two bands or the induced tunnelling, as outlined above. Finally, the lattice has a slightly shorter lattice spacing $|\mathbf{v}_0| = 0.438 \lambda$ along x , implying that the bond angle departs from 90° . The tunnelling parameters of the static lattice used in this paper are reproduced in Tab. S1.

As a result of $|\mathbf{v}_0| \neq |\mathbf{v}_3|$, $t'_3{}^{\text{eff}} \neq 0$. Moreover, the NN tunnellings t_j are renormalized slightly differently when modulating, as the projections in Eq. (S19) depend on the orientation and length of the tunnelling vectors. When the modulation trajectory is not circular, this weakly breaks the $x \mapsto -x$ reflection symmetry of the lattice, leading to a displacement of the Dirac points away from the $q_x = 0$ line of the Brillouin-zone, see Fig. S10. However for $\varphi = 0^\circ$ or $\pm 180^\circ$, this only amounts to a movement of the Dirac point by about 1% of the Brillouin-zone size. This effect creates a slight φ depen-

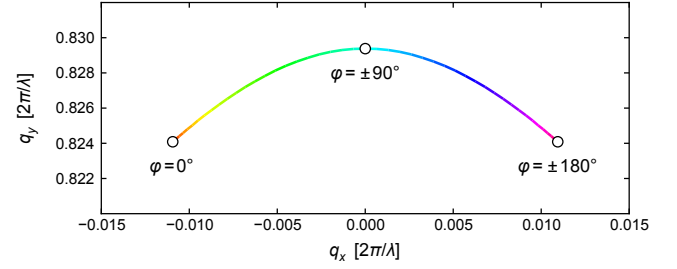


FIG. S10: Trajectory of one of the two Dirac points in quasi-momentum space when φ is varied, for $\omega = 2\pi \times 4000$ Hz, $K_0 = 0.7778$ (the other Dirac point is located at opposite quasi-momentum).

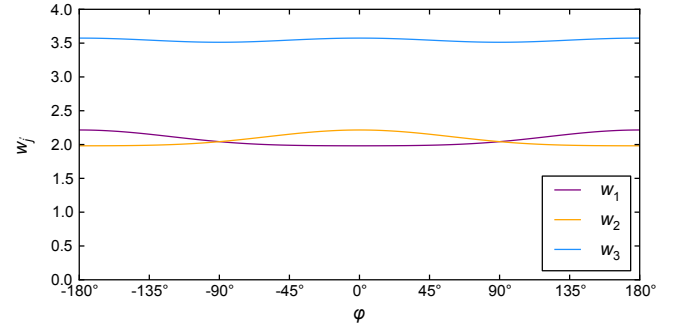


FIG. S11: Weights w_j relating imaginary next-nearest neighbour tunnelling to the gap Δ_T , as a function of φ .

dence for the weights w_j in Eq. (S29), see Fig. S11.

At a modulation frequency $\omega = 2\pi \times 4000$ Hz and an amplitude $K_0 = 0.7778$, the maximum gap is achieved for circular modulation and is numerically computed to be $\hbar \times 88$ Hz (analytically we find 91 Hz). Deviations from the sinusoidal dependence on φ owing to higher-order terms of the perturbative expansion remain below 2%, see Fig. S12). The calculated band-structures and Berry-

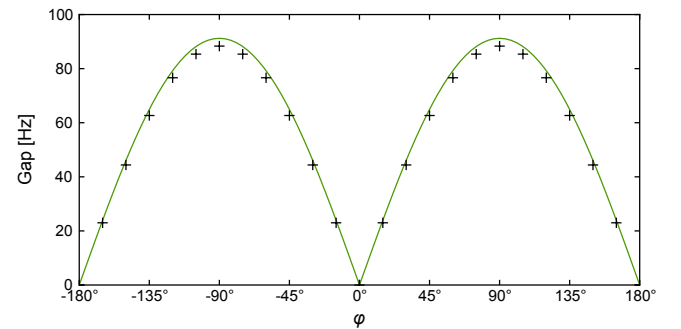


FIG. S12: Analytic (lines) and numerical (crosses) absolute gap of the experimental lattice versus relative phase φ between horizontal and vertical modulation, for $\omega = 2\pi \times 4000$ Hz, $K_0 = 0.7778$.

curvatures for our experimental parameters are shown in Fig. S13.

EXPERIMENTAL DETAILS

Drift measurements for opposite forces

In this section data for the individual drift after one full Bloch cycle supplementing Fig. 2c/d and Fig. 4 in the main text are shown. Our measurement technique probes the Berry curvature of the lowest band by moving atoms in q_y -direction past the gapped Dirac points, where the Berry curvature is localized, and relies on the coupling of real and momentum space. As described in the main text, the applied uniform force causes an orthogonal velocity in real space when atoms are in the region of the Berry curvature. The resulting change in real space position induces a transverse force arising from the underlying harmonic confinement in opposite direction of the displacement. As a result, we observe a drift in quasi-momentum, which is amplified by the negative effective mass at each Dirac point arising from the negative curvature of the band structure.

In the topologically trivial case, when only IS is broken, we observe a drift in quasi-momentum along q_x when scanning the sublattice offset Δ_{AB} (see Fig. S14). This constitutes a measure of the local Berry curvature as the total Berry curvature is zero. We measure a drift which increases with increasing gap and changes sign with Δ_{AB} . The data shows that the observed drift predominately arises from the first Dirac point which is passed. This effect can be explained in the following way. The Berry curvature of the first Dirac point already leads to an orthogonal drift in quasi-momentum. When successively reaching the second Dirac point the shifted part of the cloud then does not experience the same Berry curvature distribution. As expected, opposite oscillation directions give rise to the same drift, since not only the direction of the force changes but also the sign of the Berry curvature corresponding to the first Dirac point on the trajectory (see Fig. S14 c). Subtracting the drifts of opposite gradients gives the differential drift \mathcal{D} , as shown in the main manuscript. This probes the net contribution of both Dirac points. Only for the largest Δ_{AB} the measured drift decreases again, indicating an increasing spread of the Berry curvature distribution at each Dirac point, which then start to overlap and gradually cancel each other (see Fig. S14 b). We also observe these drifts in a static lattice with $\Delta_{AB} \neq 0$.

In contrast, when only TRS is broken, we probe the topologically non-trivial regime. Fig S15 shows opposite drifts along q_x for each of the oscillation directions. In this case both successively passed Dirac points cause a drift in the same direction since the Berry curvature is an even function of \mathbf{q} . Therefore, changing the sign

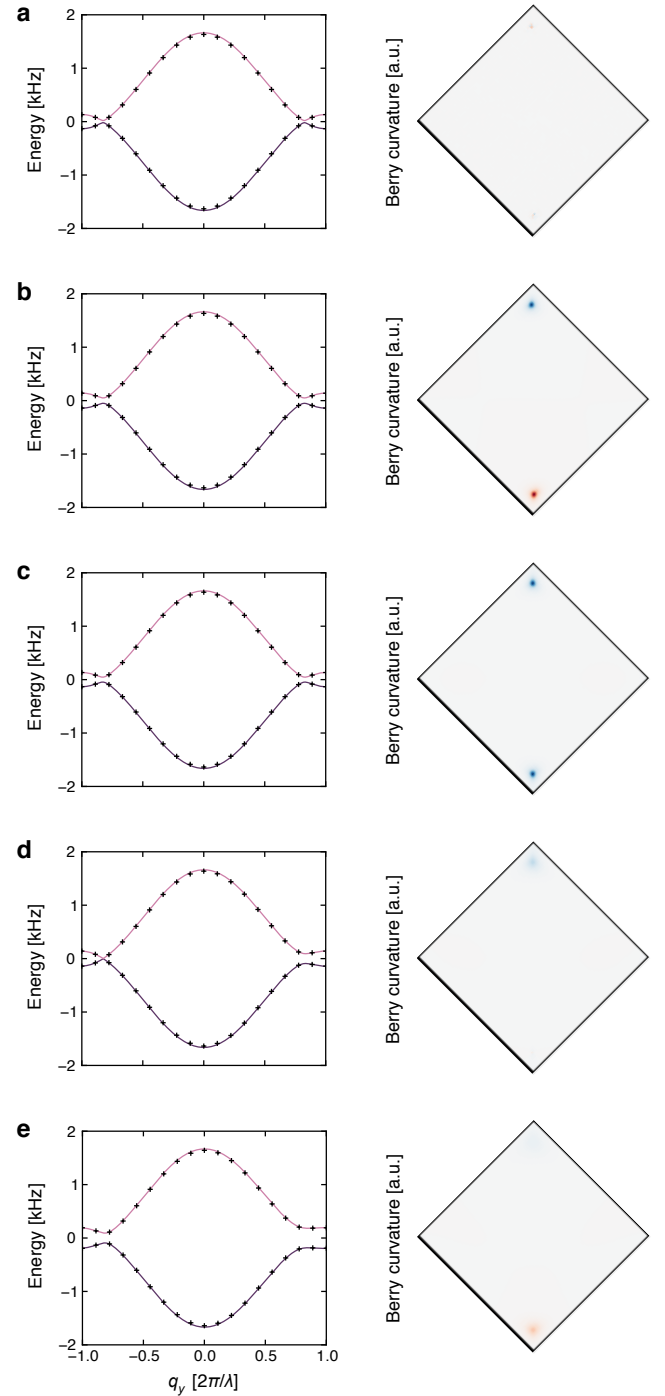


FIG. S13: Cut of the energy bands along the vertical line $q_x = 0$ and Berry curvature of the modulated realistic honeycomb lattice for $\omega = 2\pi \times 4000$ Hz, $K_0 = 0.7778$ and
a. $\varphi = 0$, $\Delta_{AB} = 0$ (IS and TRS not broken);
b. $\varphi = 0$, $\Delta_{AB} = |\Delta_T^{\max}| = h \times 88$ Hz (trivial phase, $\nu = 0$);
c. $\varphi = 90^\circ$, $\Delta_{AB} = 0$ (non-trivial phase, $\nu = -1$);
d. $\varphi = 90^\circ$, $\Delta_{AB} = |\Delta_T^{\max}|$ (topological transition);
e. $\varphi = 90^\circ$, $\Delta_{AB} = 3|\Delta_T^{\max}|$ (trivial phase, $\nu = 0$).
 The Dirac points are rotated out of the vertical in panels **a.** and **b.**, which translates to an apparent gap in the band cut of **a.** and a slightly asymmetric Berry curvature in **b.**

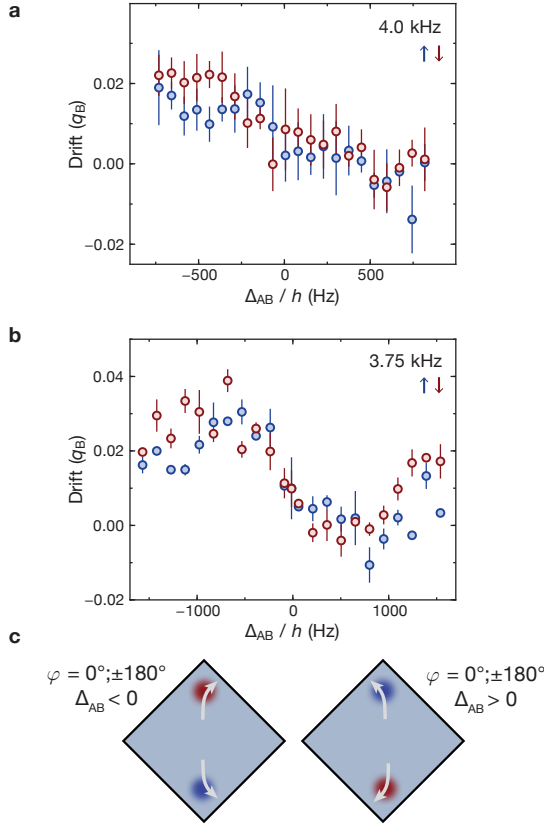


FIG. S14: **Drift measurement for broken IS.** The measured drift used to obtain the differential Drift \mathcal{D} in Fig. 2c and Fig. 4 of the main text is individually shown for positive and negative forces in the q_y -direction. **a/b**, We break IS by introducing a sublattice offset and show measurements with modulation frequency of 4.0 kHz (**a**) and 3.75 kHz (**b**). Although the opposite Berry-curvatures at the two Dirac points sum up to zero within the first BZ, we clearly see a drift depending on the size of Δ_{AB} . Data for positive (negative) force is shown in blue (red). Data show mean \pm s.d. of at least 6 (**a**) or 2 (**b**) measurements. **c**, Schematics show the expected orthogonal drifts caused by driving the atoms through the Berry curvature distribution. Red (Blue) indicate positive (negative) Berry curvature. If only IS is broken the Berry curvature distribution is an odd function of \mathbf{q} and changes sign when changing the sign of the sublattice offset. For opposite forces inducing a Bloch oscillation this leads to the same direction of the drift as indicated by the white arrows.

of the applied gradient leads to a drift in the opposite q_x -direction. As expected, the drift changes sign for the opposite modulation phase difference φ , directly revealing the changing sign of the Berry curvature distribution. Here too, a larger gap (when φ is closer to $\pm 90^\circ$ or the modulation frequency is lower) leads to a larger drift (see Fig. S13). The combination of the dependence of the drift on the size of the gap and the predominance of the first Dirac point on the trajectory may be the cause for the precursors seen in Fig 4a for simultaneously broken IS and TRS.

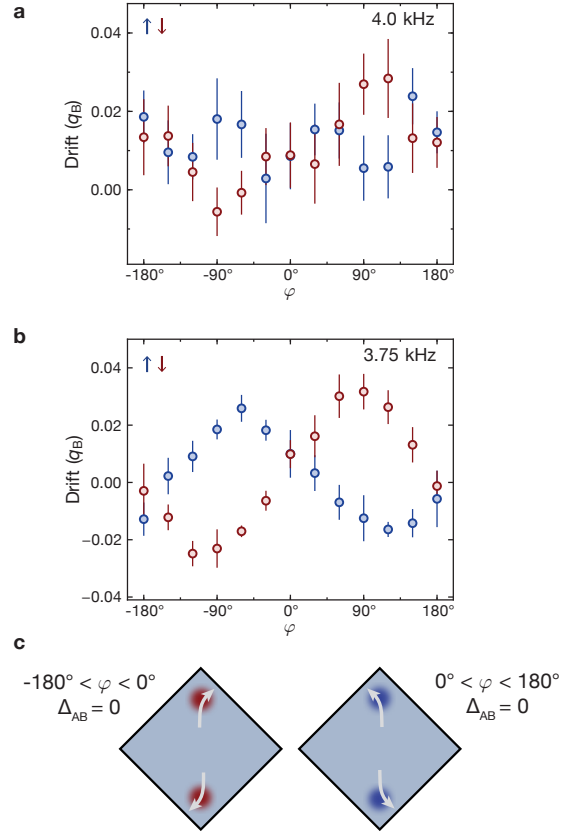


FIG. S15: **Drift measurement for broken TRS.** Individual drifts as in Fig. S14 supplementing Fig. 2d and Fig. 4 of the main text. **a/b**, By changing the modulation phase difference φ we break TRS and the system enters the topologically non-trivial regime. In this case the drift for each oscillation direction shows a different sign, which changes as expected for opposite φ . Drift data for positive (negative) force is shown in blue (red) for a modulation frequency of 4.0 kHz (**a**) and 3.75 kHz (**b**). Data show mean \pm s.d. of at least 21 (**a**) or 6 (**b**) measurements. **c**, Schematics show the expected orthogonal drifts caused by driving the atoms through the Berry curvature distribution. Red (Blue) indicate positive (negative) Berry curvature. If only TRS is broken the Berry curvature distribution at each Dirac point has the same sign, which is changed when reverting the rotation direction. In this case the opposite forces lead to opposite directions of the drift.

Heating of a repulsively interacting Fermi gas

We have also investigated the increase in entropy when loading a repulsively interacting Fermi gas in a modulated lattice of coupled honeycomb layers and reverting the loading procedure [S15, S16], and compare it to the static lattice (see Fig. S16a). For this measurement, different interaction strengths and modulation frequencies are used, while K_0 is kept constant. In the crossover regime between the metallic and the insulating phase

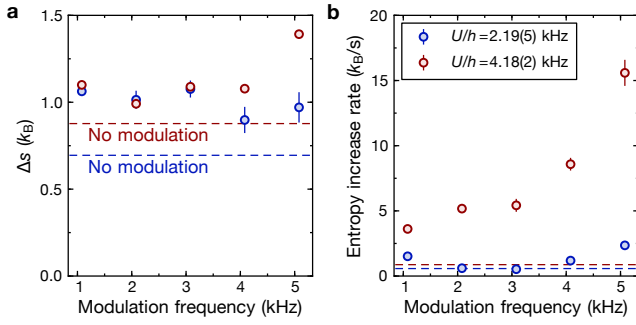


FIG. S16: (a) Entropy increase associated with loading into the modulated lattice and reverting the loading procedure and (b) entropy increase rate in the modulated lattice for long holding times. The frequency $\omega = 2\pi \times 1080$ Hz opens a gap of $h \times 44$ Hz in the non-interacting band-structure, similar, in units of the tunnelling, as in the measurements of the main text. The dashed line shows the measured heating in a lattice without modulation with identical interaction strengths.

($U/h = 2.19(5)$ kHz), the higher entropy increase possibly originates from the presence of low-energy charge excitations. Furthermore, in the insulating phase, we cover the doublon excitation peak, whose frequency is given by $U/h = 4.18(2)$ kHz. Note that the modulation frequency of 1.08 kHz is the same in proportion to the bandwidth as in the measurements of the main text, and opens a similar gap in proportion to the tunnelling. Moreover, we have measured the additional heating induced by holding the atoms in the modulated lattice for a varying time (see Fig. S16b). For experimentally relevant durations, this contribution is comparable to the first one. We find that the heating induced by the modulation does not dominate the final temperature, thus demonstrating that the scheme is well suited for studying of many-body states in topological lattices.

- [S1] Haldane, F. D. M. Model for a Quantum Hall Effect without Landau Levels: Condensed-Matter Realization of the "Parity Anomaly". *Phys. Rev. Lett.* **61**, 2015–2018 (1988).
- [S2] Eckardt, A., Weiss, C. & Holthaus, M. Superfluid-insulator transition in a periodically driven optical lattice. *Phys. Rev. Lett.* **95**, 260404 (2005).
- [S3] Oka, T. & Aoki, H. Photovoltaic Hall effect in graphene. *Phys. Rev. B* **79**, 081406 (2009).
- [S4] Kolovsky, A. R. Creating artificial magnetic fields for cold atoms by photon-assisted tunneling. *Europhys. Lett.* **93**, 20003 (2011).
- [S5] Lebrat, M. *Engineering artificial gauge fields in time-modulated optical lattices*. Master's thesis, ETH Zürich (2013).
- [S6] Delplace, P., Gómez-León, A. & Platero, G. Merging of Dirac points and Floquet topological transitions in ac-driven graphene. *Phys. Rev. B* **88**, 245422 (2013).
- [S7] Goldman, N. & Dalibard, J. Periodically-driven quantum systems: Effective Hamiltonians and engineered gauge fields. *arXiv e-prints* (2014). 1404.4373.
- [S8] Grushin, A. G., Gómez-León, A. & Neupert, T. Floquet Fractional Chern Insulators. *Phys. Rev. Lett.* **112**, 156801 (2014).
- [S9] Zheng, W. & Zhai, H. Floquet Topological States in Shaking Optical Lattices. *arXiv e-prints* (2014). 1402.4034.
- [S10] Shirley, J. H. Solution of the Schrödinger equation with a Hamiltonian periodic in time. *Phys. Rev.* **138**, B979–B987 (1965).
- [S11] Sambe, H. Steady states and quasienergies of a quantum-mechanical system in an oscillating field. *Phys. Rev. A* **7**, 2203–2213 (1973).
- [S12] Rahav, S., Gilary, I. & Fishman, S. Effective Hamiltonians for periodically driven systems. *Phys. Rev. A* **68**, 013820 (2003).
- [S13] Xiao, D., Chang, M.-C. & Niu, Q. Berry phase effects on electronic properties. *Rev. Mod. Phys.* **82**, 1959–2007 (2010).
- [S14] Kitagawa, T., Berg, E., Rudner, M. & Demler, E. Topological characterization of periodically driven quantum systems. *Phys. Rev. B* **82**, 235114 (2010).
- [S15] Uehlinger, T. *et al.* Artificial Graphene with Tunable Interactions. *Phys. Rev. Lett.* **111**, 185307 (2013).
- [S16] Greif, D., Tarruell, L., Uehlinger, T., Jördens, R. & Esslinger, T. Probing nearest-neighbor correlations of ultracold fermions in an optical lattice. *Phys. Rev. Lett.* **106**, 145302 (2011).